# Dynamic Bayesian Networks for Modelling Chemical Degradation in Concrete Structures of Nuclear Waste Repositories Exposed to Climate Change

*Seyed Ali Hosseini* [a], *Giovanni Roma* [a], *Francesco Di Maio* [a*], *Enrico Zio* [a, b]

[a] Energy Department, Politecnico di Milano, Via La Masa 34, Milano 20156, Italy

[b] Mines Paris, PSL Centre de Recherche sur les Risques et les Crises, Sophia Antipolis 06904, France

***Corresponding author:** *E-mail address: francesco.dimaio@polimi.it*

---

## Abstract

Concrete is the ultimate engineering barrier that prevents the release of radioactive contaminants from Nuclear Waste Repositories (NWRs). Concrete suffers from two main chemical degradation processes that are expedited by Climate Change (CC): carbonation-induced corrosion and chloride ingress. Climatic variables, like temperature, relative humidity, and $CO_2$ concentration, have an impact on the process of chemical degradation of concrete; this impact is uncertain, as it depends on the evolution of CC.

In this work, we use Dynamic Bayesian Networks (DBNs) to model concrete chemical degradation, within the Performance Assessment (PA) of NWRs, and considering the effects of CC. The DBN models are applied to assess aquifer contamination, due to CC-induced concrete degradation, and dose intake from a realistic near-surface NWR. The results obtained show that the severe CC scenario (SSP-5 8.5) leads to the largest levels of concrete degradation and dose intake, as CC-induced degradation processes exceed the critical thresholds about a decade sooner than for moderate and low-emission scenarios. Moreover, as expected, deep uncertainty in CC variables significantly broadens the tolerance intervals of dose-intake violation probabilities, exposing long-term risk-informed PA to larger uncertainty, that are to be duly considered.

**Keywords:** *Nuclear Waste Repository, Performance Assessment, Concrete Corrosion, Aquifer Contamination, Climate Change, Deep Uncertainty, Residual Uncertainty, Dynamic Bayesian Network (DBN).*

## Nomenclature

### Acronyms

| | |
|---|---|
| **BDeu** | Bayesian Dirichlet–equivalent uniform |
| **BN** | Bayesian Network |
| **BT** | Bow-Tie |
| **CC** | Climate Change |
| **CD** | Chemical Degradation |
| **CMIP6** | Coupled Model Intercomparison Project Phase 6 |
| **CPTs** | Conditional Probability Tables |
| **$CO_2$** | Carbon-dioxide Concentration |
| **COV** | Coefficient of Variation |
| **DAG** | Directed Acyclic Graph |
| **DBNs** | Dynamic Bayesian Networks |
| **DI** | Dose Intake |
| **FT** | Fault Tree |
| **GCM** | Global Climate Model |
| **FEP** | Features, Events and Process |
| **IPCC** | Intergovernmental Panel on Climate Change |
| **MAP** | Maximum a Posteriori |
| **MC** | Mote-Carlo |
| **MFM** | Multilevel Flow Modeling |
| **MLE** | Maximization Likelihood Estimation |
| **NPP** | Nuclear Power Plant |
| **PA** | Performance Assessment |
| **PRA** | Probabilistic Risk Assessment |
| **T** | Temperature |
| **RH** | Relative Humidity |
| **RCPs** | Representative Concentration Pathways |
| **RCMs** | Regional Climate Models |
| **RAMS** | Reliability, Availability, Maintainability and Safety |
| **RIC** | Residual Interval Characterization |
| **GHGs** | Green-House Gases |
| **SSPs** | Shared Socioeconomic Pathways |
| **UQ** | Uncertainty Quantification |

### Symbols

| | |
|---|---|
| $\tau$ | Time slice |
| $p$ | Index of the CC variable |
| $q$ | Index of the FEP |
| $u$ | State identifier index |
| $m$ | Index of the combinations of parent |
| $\alpha$ | Total number of hypothetical prior observations |
| $\beta$ | Confidence |
| $\gamma$ | Coverage |
| $N_\gamma^\beta$ | Number of the samples to be used in Wilk's formula to estimate $\gamma$-th percentile of a distribution with confidence $\beta$ |
| $X_p(\tau)$ | The $p$-th CC variable at time $\tau$ |
| $\boldsymbol{X}(\tau)$ | Vector of all CC variables at time $\tau$ |
| $Y_q(\tau)$ | The node of $q$-th FEP at time $\tau$ |
| $\boldsymbol{Y}(\tau)$ | Vector of all FEPs at time $\tau$ |
| $Y_Q(\tau)$ | The safety target node at time $\tau$ |
| $X_T$ | Temperature |
| $X_{RH}$ | Relative humidity |
| $X_{CO_2}$ | $CO_2$ concentration |
| $Y_C$ | Carbonation FEP |
| $Y_{Cl}$ | Chloride ingress FEP |
| $\boldsymbol{Y}^{exp}(\tau)$ | FEPs determined by expert elicitation at time $\tau$ |
| $\boldsymbol{Y}^{sim}(\tau)$ | FEPs determined by physical model at time $\tau$ |
| $Y_Q^{threshold}$ | Threshold value for safety target |
| $V_i$ | The $i$-th node of DBN |
| $V_T$ | Temperature node |
| $V_{RH}$ | Relative humidity node |
| $V_{CO_2}$ | $CO_2$ concentration node |
| $V_C$ | Carbonation node |
| $V_{Cl}$ | Chloride ingress node |
| $V_{CD}$ | Chemical degradation node |
| $V_{DI}$ | Dose Intake node |
| $\boldsymbol{V}$ | All nodes of DBN |
| $\boldsymbol{V^D}$ | Dependent nodes |
| $\boldsymbol{V^I}$ | Independent nodes |
| $\boldsymbol{V}_-^i$ | Parent nodes of the $i$-th node |
| $A$ | Vector of all arcs (edges) of DBN |
| $s_{i,u}$ | The $u$-th state of $i$-th node ($V_i$) |
| $\boldsymbol{S}_i$ | All states of $V_i$ |
| $\boldsymbol{S}_{i(m)}^-$ | The $m$-th combination of parents' states of $V_i$ |
| $\boldsymbol{S}_i^-$ | Set of combinations of the parents' nodes of $V_i$ |
| $\boldsymbol{s}_{-i}$ | A combination of nodes' states expects $i$-th node ($V_i$) |
| $\boldsymbol{S}_{-i}$ | All combinations of nodes' states expect $i$-th node ($V_i$) |
| $P_{vio}(\tau)$ | Violation probability of the safety threshold at time $\tau$ |
| $\hat{P}_{MC}^C(\tau)$ | MC point estimate of the exceedance probability |

| | | | |
|---|---|---|---|
| | node states | | of carbonation corrosion at time $\tau$ |
| $c_i$ | Total number of states for the $i$-th node ($V_i$) | $\hat{P}_{MC}^{Cl}(\tau)$ | MC point estimate of the exceedance probability of Chloride ingress at time $\tau$ |
| $d_i$ | Total number of combinations of the parent node states for the $i$-th node ($V_i$) | $\hat{P}_{MLE}^{C}(\tau)$ | MLE point estimate of the exceedance probability of carbonation corrosion at time $\tau$ |
| $n_{tot}$ | Number of the DBN's nodes | $\hat{P}_{MLE}^{Cl}(\tau)$ | MLE point estimate of the exceedance probability of Chloride ingress at time $\tau$ |
| $Q_{exp}$ | Number of the expert-based FEPs | $\hat{P}_{MLE}^{vio}(\tau)$ | MLE point estimate of the violation probability at time $\tau$ |
| $Q_{sim}$ | Number of the simulated FEPs | $\boldsymbol{p}(P_{vio}(\tau))$ | Distribution of the violation probability at time $\tau$ |
| $\mathrm{T}_\tau$ | Total number of the time slices | $\underline{P_{vio}}(\tau)$ | Lower bound of the violation probability at time $\tau$ |
| $\boldsymbol{\mathcal{D}}$ | Training dataset ($\boldsymbol{\mathcal{D}}_{dat}$ and $\boldsymbol{\mathcal{D}}_{sim}$) | $\overline{P_{vio}}(\tau)$ | Upper bound of the violation probability at time $\tau$ |
| $\boldsymbol{\mathcal{D}}_{dat}$ | Training dataset used for learning the CPT parameters by CC data | $\overline{P_C}(\tau)$ | Upper bound of the exceedance probability of the carbonation corrosion at time $\tau$ |
| $\boldsymbol{\mathcal{D}}_{sim}$ | Training dataset used for learning the CPT parameters by physical model simulations | $\overline{P_{Cl}}(\tau)$ | Upper bound of the exceedance probability of the chloride ingress at time $\tau$ |
| $N_{dat}$ | Total number of CMIP6 available models (rows of $\boldsymbol{\mathcal{D}}_{dat}$) | $\overline{P_C^{boot}}(\tau)$ | Upper bound of the exceedance probability of the carbonation corrosion at time $\tau$ using the bootstrap-based tolerance interval |
| $N_{sim}$ | Total number of simulation dataset (rows of $\boldsymbol{\mathcal{D}}_{sim}$) | $\overline{P_{Cl}^{boot}}(\tau)$ | Upper bound of the exceedance probability of the chloride ingress at time $\tau$ using the bootstrap-based tolerance interval |
| $N_{MC}$ | Number of Monte-Carlo simulations | $\mathbf{p}^{dat}$ | CPTs' parameters learned from CC-variables projections data |
| $\omega_{D\|\boldsymbol{S}_{i(m)}^-}$ | Normalization factor of Dirichlet distribution function for training data ($\boldsymbol{\mathcal{D}}_{\boldsymbol{dat}}$ and $\boldsymbol{\mathcal{D}}_{\boldsymbol{sim}}$) given $\boldsymbol{S}_{\boldsymbol{i}(m)}^-$ | $\mathbf{p}^{sim}$ | CPTs' parameters learned from CC-variables projections data |
| $\alpha_{s_{i,u}\|\boldsymbol{S}_{i(m)}^-}$ | Hyperparameters of Dirichlet distribution reflects the number of times an expert expects to observe the event $\left(V_i = s_{i,u}\middle\|\boldsymbol{V}_i^- = \boldsymbol{S}_{i(m)}^-\right)$ | $p_{s_{i,u}}$ | The state probability of $s_{i,u}$ for $i$-th independent node ($\Pr(V_i = s_{i,u})$) |
| $N_{s_{i,u}\|\boldsymbol{S}_{i(m)}^-}$ | Number of the observed training samples state $s_{i,u}$ given $\boldsymbol{S}_{\boldsymbol{i}(m)}^-$ | $P_C(\tau)$ | Probability of carbonation corrosion exceedance at time $\tau$ |
| $E[.]$ | Posterior mean | $P_{Cl}(\tau)$ | Probability of chloride corrosion exceedance at time $\tau$ |
| $MAP(.)$ | Posterior mode (MAP estimate) | $p_{s_{i,u}\|\boldsymbol{S}_{i(m)}^-}$ | The conditional probability vector of $i$-th node given parents' states $\boldsymbol{S}_{\boldsymbol{i}(m)}^-$ ($\Pr(V_i = s_{i,u}\|\boldsymbol{V}_i^- = \boldsymbol{S}_{\boldsymbol{i}(m)}^-)$) |
| $x_c$ | Carbonation depth | $p_{s_i\|\boldsymbol{S}_{i(m)}^-}\|\boldsymbol{\mathcal{D}}$ | Posterior distribution of $\boldsymbol{p}_{s_i\|\boldsymbol{S}_{i(m)}^-}$ given $\boldsymbol{\mathcal{D}}$ |
| $C(x,\tau)$ | Chloride ion concentration at depth $x$ and time $\tau$ | $\alpha_H$ | Content of hydrogen |
| $C_{Critical}$ | Critical concentration of chloride ingress | $n_d$ | Aging factor of $D_0^C$ |
| $D_0^C$ | Initial $CO_2$ diffusion coefficient | $n$ | Aging factor of $D_0^{Cl}$ |
| $D_0^{Cl}$ | Initial chloride ion diffusion coefficient | $n_m$ | Exposure factor for microclimatic wetting ang drying cycles |
| $f_T^C(\tau)$ | Temperature correction factor for $CO_2$ diffusion coefficient at time $\tau$ | $C_{CO_2}$ | Mass concentration of $CO_2$ in the environment |
| $f_{RH}^C(\tau)$ | Relative humidity correction factor for $CO_2$ diffusion coefficient at time $\tau$ | $C_e$ | Cement content |
| $f_T^{Cl}(\tau)$ | Temperature correction factor for chloride diffusion coefficient at time $\tau$ | $C_aO$ | CaO content in the cement |
| $f_{RH}^{Cl}(\tau)$ | Relative humidity correction factor for chloride diffusion coefficient at time $\tau$ | $k_{site}$ | Increase factor of $CO_2$ concentration in industrial or urban areas |
| $^w/_c$ | Water to cement ratio | $k_e$ | Environmental factor for chloride diffusion coefficient |
| $M_{CO_2}$ | Molar mass of $CO_2$ | $k_t$ | Test method factor for chloride diffusion |

| | | | |
|---|---|---|---|
| | | | coefficient |
| $M_{C_aO}$ | Molar mass of CaO | | |
| $\mathcal{G}$ | The structure of DAG | | |
| $\Delta t$ | Duration between two time slices $t_{\tau+1}$ and $t_\tau$ | $k_c$ | Cutting factor for chloride diffusion coefficient |

## 1. Introduction

Nuclear facilities produce hazardous radioactive waste that must be confined to protect humans and the environment. This can be done in Nuclear Waste Repositories (NWRs) [1], whose safety is evaluated through a Performance Assessment (PA) [2]. PA must be performed considering the negative effects that Climate Change (CC) could have in the future on the repository concrete structures [3], through changes of climatic variables such as precipitation and temperature [4]. These changes may be such to expedite chemical degradation of concrete, thus increasing the risk of groundwater contamination, and ultimately harm to humans [5-9]. In particular, the degradation of the repository concrete barriers is due to two main time-dependent chemical processes, i.e., carbonation and chloride ingress [10, 11], that are influenced by temperature, relative humidity, and $CO_2$ concentration. Conducting a PA, thus, requires a framework of analysis capable of: (i) representing the temporal evolution of both climatic variables and degradation processes over the multi-decadal timescales relevant to NWR safety assessment; (ii) capturing causal dependencies between climatic variables and concrete degradation mechanisms; (iii) handling the deep uncertainty inherent to climate projections; and (iv) integrating heterogeneous information sources including physics-based concrete degradation models, climate projection datasets, and expert judgment. Traditional probabilistic methods present limitations in meeting these requirements: Monte Carlo simulation, while widely used in PA [12, 13], treats the NWR model as a black box and does not explicitly represent causal relationships, making it difficult to update assessments as new climate data becomes available or to trace the impact of specific CC variables on PA outcomes; Fault Tree (FT) [14] and Event Tree [15] methods, commonly employed in nuclear safety analysis, are limited by the Boolean logic therein, so that NWR barriers can only be modelled by binary states and do not naturally accommodate the continuous temporal evolution of their degradation processes; standard (static)

Bayesian Networks (BNs) [16] can represent causal dependencies and handle multi-state variables but lack the ability to model time-sequential dependencies that are fundamental to concrete degradation under evolving climate conditions.

In this work, Dynamic Bayesian Networks (DBNs) are employed for degradation modeling within PA [17], as they address the aforementioned limitations by extending static BNs to the temporal domain. DBNs have been used in several reliability, availability, maintainability and safety (RAMS) applications, including prognostic and health management [18-20], risk and resilience analysis of complex systems [18-20], risk-informed decision making [21, 22], chemical process risk assessment [23-25], maintenance planning of structures [26], and portfolio optimization of safety measures [27]. In recent years, several studies have further adopted BN/DBNs for nuclear systems and critical infrastructure analyses [28]. In the nuclear field, BNs have been adopted for fault diagnostic [29], human reliability analysis [30, 31], seismic Probabilistic Risk Assessment (PRA) [32, 33], and real-time severe accident management [34, 35]. Recent studies have also shown the capability of DBNs to model deterioration of concrete structures [36-38]. Unlike BNs, DBNs are capable of modeling temporal processes and capturing time-sequential dependencies [39]. Then, we use DBNs to account for the dependencies between the evolving CC variables and the degradation state of concrete barriers to eventually assess the effects of CC on exceeding the acceptable limits of probability on the radiation dose intake. The nodes of the DBNs represent the Features, Events and Processes (FEPs) [16], that characterize the repository and its environment, including the sink node (i.e., a node with no outgoing edges) related to the safety parameter of interest, e.g., the probability that the dose intake violates the acceptable safety threshold value. The DBN nodes are connected by edges that indicate conditional dependences, quantified using Conditional Probability Tables (CPTs) whose estimates can be assigned through expert elicitation [40] or learned from data (e.g., through Maximum Likelihood Estimation (MLE) [41]). In the latter case, different sources of data can be used, such as climate projection datasets (e.g., CMIP6 [42-44]) for the nodes of CC variables (e.g., temperature, relative humidity and $CO_2$ concentration), or datasets generated through physical

models that simulate the time-dependent chemical degradation processes of concrete by carbonation-induced corrosion and chloride ingress [10, 17, 45].

In practice, CC variables projections are affected by deep uncertainty, which is typically characterized as [46]: *scenario uncertainty* (i.e., related to the unpredictability of future human activities, including greenhouse gas emissions and land-use changes), *model uncertainty* (i.e., related to how different climate models lead to different projections under the same input conditions) and *internal variability uncertainty* (i.e., related to the natural, unpredictable climate fluctuations that occur also without external influences like greenhouse gases, solar changes, etc.). Both SSP scenario uncertainty and climate model uncertainty are considered epistemic, as they arise from incomplete knowledge of future socio-economic pathways and imperfect representations of the climate system, respectively. The relative importance of these sources of uncertainty on the CC variables values depends on the time scales of the analysis: for decadal time scales (i.e., over 20 to 30 years in the future) the contributions of *scenario uncertainty* and *model uncertainty* are expected to be the most important ones [46] to be considered in the PA of NWRs. S*cenario uncertainty* is typically addressed considering different Shared Socioeconomic Pathways (SSPs) (i.e., scenarios describing possible future societal trends that influence greenhouse gas emissions and climate change impacts) [47]. For a given SSP scenario, *model uncertainty* is addressed by considering multiple climate models (e.g., those compared and analyzed in the Coupled Model Intercomparison Project Phase 6 (CMIP6) [44]) and the spread among their respective projections.

Another source of epistemic uncertainty stems from the incompleteness of the set of physical model simulations adopted to estimate the CPTs of the DBN, at the time of the analysis is carried out. This uncertainty, extensively discussed in [16], impacts on the DBN outcomes and, therefore, should be attentively considered.

In this work, we propose a DBN-based modeling framework to account for the impact of *scenario uncertainty* and *model uncertainty* within PA of NWRs. Specifically, scenario uncertainty is addressed by

developing a DBN for each SSP scenario considered, whereas model uncertainty and the uncertainty that arises from the incompleteness of physical model simulations are considered within the uncertainty of CPTs parameters [16] and propagated through the DBNs to quantify the uncertainty on the outcomes. Methods for characterizing the uncertainty of CPTs parameters are either based on *probability* theory or on *interval-valued* uncertainty [48]. For the former, for example, the uncertainty on CPTs parameters can be assumed to follow a Dirichlet probability distribution (or a Beta distribution for binary nodes), and through Monte Carlo sampling the residual uncertainty in the DBN output is characterized. For the latter, the uncertainty in the CPTs parameters is represented by intervals of variability, which are then propagated to characterize the residual uncertainty of the outputs by solving optimization problems over the sets of probabilities [48]; however, in this latter case, the computational complexity and time required for the inference process can become intractable for complex networks (i.e., networks characterized by a large number of nodes and high tree-width) [49, 50]. For this reason, in this paper, we opt for a probabilistic representation of the uncertainty in the CPTs values and a Residual Interval Characterization (RIC) non-parametric tolerance interval method [48].

The resulting modelling framework is applied to a near-surface NWR located in Dessel, Belgium [16, 51, 52], for a time-dependent probabilistic analysis of dose intake accounting for scenario and model uncertainty in relation to three different SSPs scenarios, namely, SSP-1 2.6, SSP-2 4.5, and SSP-5 8.5 (i.e., limiting global temperature increase to 2℃, 3℃, and 4℃, due to low, intermediate and very high emissions of GHGs (Green-House Gases), respectively) and the projections of the CMIP6 climatic models as in [53].

To the best of the authors' knowledge, this is the first DBN-based modelling framework proposed for the PA of NWRs that explicitly aims to represent deep climate change uncertainty. Specifically, the methodological advancements of the proposed framework include: (i) explicit representation and incorporation of deep uncertainty arising from both scenario and model uncertainty in CMIP6 climate projections; (ii) development of Residual Interval Characterization (RIC) as a non-parametric tolerance-

interval approach to account for epistemic uncertainty in CPT parameterization of the DBN-based modelling framework; (iii) application of a combined parameter-learning algorithm that integrates limited CMIP6 data and physical simulation datasets within a unified framework; (iv) consideration of two connected degradation processes (carbonation and chloride ingress) to establish a logical joint chemical degradation state for concrete barriers; and (v) application of the DBN-based modelling framework to a realistic near-surface NWR.

The remaining Sections of the manuscript are structured as follows: Section 2 formulates the DBN modeling framework that embeds CC variables projections, and the method for CPTs uncertainty quantification and propagation, Section 3 describes the case study and Section 4 presents the results. In Section 5, conclusions are drawn.

## 2. DBN Modelling of Concrete Degradation

A discrete-time model of concrete degradation is developed, considering a finite set of uniformly spaced time steps $[0, 1, \dots, \tau, \dots, T_\tau]$, each of duration $\Delta t = t_{\tau+1} - t_\tau$. Let $\boldsymbol{Y}(\tau) = \{Y_1(\tau), \dots, Y_q(\tau), \dots, Y_Q(\tau)\}$ be the set of FEPs variables that characterize the degradation process at the generic time step $\tau$ (e.g., the carbonation depth due to carbonation-induced corrosion or the chloride concentration), $Y_Q(\tau)$ be the safety target (e.g., the dose rate to the public), and $\boldsymbol{X}(\tau) = \{X_1(\tau), \dots, X_p(\tau), \dots, X_P(\tau)\}$ be the set of CC climatic variables considered to influence the degradation of concrete (e.g., temperature, relative humidity, and $CO_2$).

BNs have already been used to model the causal interdependencies among FEPs for the PA of NWRs [16]. In this Section, we propose a DBN to model the dynamic evolution of the NWR FEPs under the effects of CC climatic variables, over discrete time slices $\tau = 0,1, \dots, T_\tau$.

The development of the DBN consists of three steps: variables selection, structure modeling and parameter modeling.

Variables selection aims at identifying the set of CC climatic variables $\boldsymbol{X}(\tau)$ and FEPs $\boldsymbol{Y}(\tau)$ characterizing the degradation process. Then, each element $X_p(\tau) \in \boldsymbol{X}(\tau)$ and $Y_q(\tau) \in \boldsymbol{Y}(\tau)$ is associated with a corresponding node in the DBN, such that the total number of DBN nodes $n_{tot}$ is:

$$n_{tot} = (P + Q) \cdot (T_\tau + 1) \tag{1}$$

Structure Modeling aims at defining the causal conditional dependencies among the DBN nodes through a Directed Acyclic Graph (DAG) $\mathcal{G}$ [54]. This is typically done either by expert judgment, encoding explicit cause-effect relationships, or by established mapping algorithms (e.g., Fault Tree (FT) [55], Bow-Tie (BT) models [56], and Multilevel Flow Modeling (MFM) [57]), or by structure-learning algorithms [54]. The generic DBN structure shown in Fig. 1, enables modelling: i) the causal dependencies between CC climatic variables (blue nodes) and the FEPs (orange nodes), and ii) the causal dependencies among the FEPs (including those of the target sink,  node in red) so that both intra-slice dependencies (i.e., causal dependencies within the same DBN time slice, represented by solid arrows) and inter-slice dependencies (i.e., causal dependencies across different time slices, represented by dashed arrows) are captured.

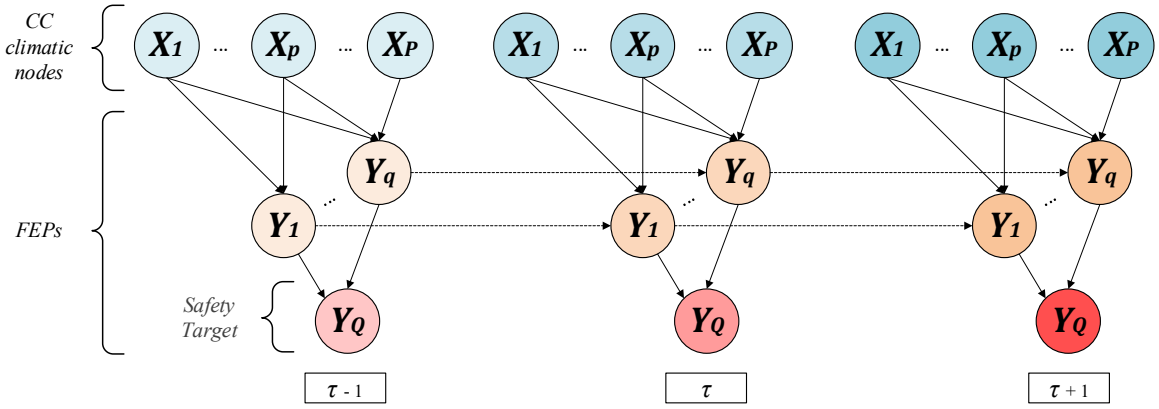


Fig. 1. DBN structure for modelling the effects of CC climatic variables on the FEPs, unrolled over three consecutive time steps.

Parameter modeling aims at characterizing the conditional dependencies among the nodes by defining the CPTs parameters. This can be done by knowledge elicitation from experts [40] or by parameter identification algorithms (e.g., MLE and Bayesian estimation) [54].

The DBN is used to compute the probability that, at a given time step $\tau$, the safety target (or any other variable of interest) violates a given safety threshold (i.e., $P_{vio}(\tau) = \Pr(Y_Q(\tau) > Y_Q^{threshold})$. However, the computed value of $P_{vio}(\tau)$, depends on the uncertain CC variable projections that make the CPTs parameters uncertain. Such uncertainty propagates into $P_{vio}(\tau)$ and determines its *residual uncertainty*, characterized by the probability distribution $p\big(P_{vio}(\tau)\big)$.

In this work, we propose a methodological framework to quantify $p\big(P_{vio}(\tau)\big)$ using a tolerance interval $\left[\underline{P_{vio}}(\tau), \overline{P_{vio}}(\tau)\right]_{\gamma}^{\beta}$, where $\underline{P_{vio}}(\tau)$ and $\overline{P_{vio}}(\tau)$ satisfy the condition $\Pr\left(\int_{\underline{P_{vio}}(\tau)}^{\overline{P_{vio}}(\tau)} p\big(P_{vio}(\tau)\big)\, dP_{vio} > \gamma\right) = \beta$, and $\gamma$ and $\beta$ are the coverage and its confidence, respectively.

## 2.1 Accounting for CC deep uncertainty in DBN-based modelling of concrete degradation

Let $\boldsymbol{V} = \{V_i | i = 1, \dots, n_{tot}\}$ be the set of the DBN nodes used for PA and $\boldsymbol{A} = \{(j,i) | V_i, V_j \in \boldsymbol{V}\}$ the set of directed edges of the DBN, where $(j,i)$ indicates an edge from node $V_j$ to node $V_i$. Let $\boldsymbol{S_i} = \{s_{i,1}, \dots, s_{i,u}, \dots, s_{i,c_i}\}$ be the set of possible states of $V_i$ (e.g., $\boldsymbol{S_i} = \{low, medium, high\}$), $\boldsymbol{V_i^-} = \{V_j \in \boldsymbol{V} | (j,i) \in \boldsymbol{A}\}$ the set of parent nodes of $V_i$, $\boldsymbol{S_i^-} = \{\boldsymbol{S_{i(1)}^-}, \dots, \boldsymbol{S_{i(m)}^-}, \dots, \boldsymbol{S_{i(d_i)}^-}\}$ the set of combinations of the parents nodes of $V_i$ given by the Cartesian product of sets $\boldsymbol{S_i^-} = \prod_{V_j \in \boldsymbol{V_i^-}} \boldsymbol{S_j}$, where $\boldsymbol{S_{i(m)}^-}$ represents the $m$-th combination of parents nodes states, with $m = 1, \dots, d_i$ and $d_i = \prod_{V_j \in \boldsymbol{V_i^-}} c_j$. For example, for $\boldsymbol{V_i^-} = \{V_1, V_2\}$, $\boldsymbol{S_1} = \{s_{1,1}, s_{1,2}\}$ and $\boldsymbol{S_2} = \{s_{2,1}, s_{2,2}\}$, $\boldsymbol{S_i^-}$ is given by $\boldsymbol{S_i^-} = \big\{\big(s_{1,1}, s_{2,1}\big), \big(s_{1,1}, s_{2,2}\big), \big(s_{1,2}, s_{2,1}\big), \big(s_{1,2}, s_{2,2}\big)\big\}$. Nodes can be independent, $\boldsymbol{V^I} = \{V_i | V_i \in \boldsymbol{V}, \boldsymbol{V_i^-} = \emptyset\}$ (i.e., nodes without parents, also known as root nodes), or dependent, $\boldsymbol{V^D} = \{V_i | V_i \in \boldsymbol{V}, \boldsymbol{V_i^-} \neq \emptyset\}$ (i.e., nodes with parents, also known as child nodes), so that $\boldsymbol{V^D} = \boldsymbol{V} \backslash \boldsymbol{V^I}$.

Let $p_{s_{i,u}} = \Pr(V_i = s_{i,u})$ be the probability that an independent node $V_i \in \boldsymbol{V^I}$ is in state $s_{i,u}$ (where $\sum_u p_{s_{i,u}} = 1$), and $p_{s_{i,u}|\boldsymbol{s_{i(m)}^-}} = \Pr(V_i = s_{i,u} | \boldsymbol{V_i^-} = \boldsymbol{S_{i(m)}^-})$ be the probability that a dependent node $V_i \in \boldsymbol{V^D}$ is in the state $s_{i,u}$ when the combination of its parents nodes state is $\boldsymbol{S_{i(m)}^-}$ (where $\sum_u p_{s_{i,u}|\boldsymbol{s_{i(m)}^-}} = 1$).

The joint probability distribution of the system state $p(V_1 = s_{1,u}, \dots, V_{n_{tot}} = s_{n_{tot},u})$ can be written as:

$$p(V_1 = s_{1,u}, \dots, V_{n_{tot}} = s_{n_{tot},u}) = \prod_{V_i \in \boldsymbol{V^I}} p_{s_{i,u}} \prod_{V_i \in \boldsymbol{V^D}} p_{s_{i,u}|\boldsymbol{s}^-_{i(m)}} \tag{2}$$

To compute the marginal probability that a generic node $V_i$ is in its generic state $s_{i,u}$, we sum (marginalize) the joint distribution over every possible combination of the remaining nodes state $\boldsymbol{s}_{-i}$:

$$\boldsymbol{s}_{-i} = (s_1, \dots, s_{i-1}, s_{i+1}, \dots, s_{n_{tot}}) \in \boldsymbol{S}_{-i} \tag{3}$$

where $\boldsymbol{S}_{-i} = \prod_{j \neq i} \boldsymbol{S}_j$ is the Cartesian product of the state spaces of all nodes except $V_i$. Then, the marginal probability that $V_i$ is in the state $s_{i,u}$ is:

$$p(V_i = s_{i,u}) = \sum_{\boldsymbol{s}_{-i} \in \boldsymbol{S}_{-i}} p(V_1 = s_1, \dots, V_i = s_{i,u}, \dots, V_{n_{tot}} = s_{n_{tot}}) \tag{4}$$

To address the SSPs scenario uncertainty, a different DBN is developed for each SSPs scenario (i.e., SSP-1 2.6, SSP-2 4.5, and SSP-5 8.5), as illustrated in Fig. 2. In contrast, to address the CC model uncertainty, for each DBN (i.e., for each SSP scenario), the CMIP6 dataset of CC variable projections $\boldsymbol{\mathcal{D}}_{dat}$ is used to infer (with uncertainty) the CPTs parameters of CC climatic variables nodes $\mathbf{p}^{dat}$ (i.e., $\mathbf{p}^{dat} = \{p_{s_{i,u}} | V_i \in \bigcup_{\tau=0}^{\tau=T_\tau} \boldsymbol{X}(\tau)\}$), where each of the $N_{dat}$ rows of $\boldsymbol{\mathcal{D}}_{dat}$ corresponds to a prediction of $\boldsymbol{X}(\tau)$ carried out by one of the $N_{dat}$ CMIP6 climatic models available [53], and the $P \cdot (T_\tau + 1)$ columns correspond to the CC climatic variables $\bigcup_{\tau=0}^{\tau=T_\tau} \boldsymbol{X}(\tau)$. For each $\tau$ and SSP scenario, the $N_{dat}$ rows correspond to the direct outputs of the CMIP6 ensemble models, which are used without additional preprocessing so that the ensemble spread explicitly represents epistemic CMIP6 models uncertainty in the climatic variables $\boldsymbol{X}(\tau)$. For what concerns $\boldsymbol{Y}(\tau)$, we can distinguish the FEPs $\boldsymbol{Y^{exp}}(\tau) = \left\{Y_1^{exp}(\tau), \dots, Y_{Q_{exp}}^{exp}(\tau)\right\}$, whose CPTs parameters are determined through expert elicitation and the FEPs simulated through a physical model $\boldsymbol{Y^{sim}}(\tau) = \left\{Y_1^{sim}(\tau), \dots, Y_{Q_{sim}}^{sim}(\tau)\right\}$

. To address the uncertainty stemming from the incompleteness of physical model simulations, the CPTs parameters of $\boldsymbol{Y^{sim}}(\tau)$, $\mathbf{p}^{sim} = \left\{p_{s_{i,u}}, p_{s_{i,u}|\boldsymbol{s}_{i(m)}^{-}} \middle| V_i \in \cup_{\tau=0}^{\tau=T_\tau} \boldsymbol{Y^{sim}}(\tau)\right\}$, are inferred (with uncertainty) from the dataset of physical model simulations $\boldsymbol{\mathcal{D}}_{sim}$, where each of the $N_{sim}$ rows of $\boldsymbol{\mathcal{D}}_{sim}$ corresponds to a simulation carried out through the physical model, and the $Q_{sim} \cdot (T_\tau + 1)$ columns correspond to the simulated FEPs. As such, parameters related to degradation processes are treated as uncertain exogenous input parameters in the DBN-based modelling framework (see Fig. 2) and are defined according to physics-based models and experimental studies of literature (see references in Table 2). The physics-based degradation models are detailed in Appendix A.

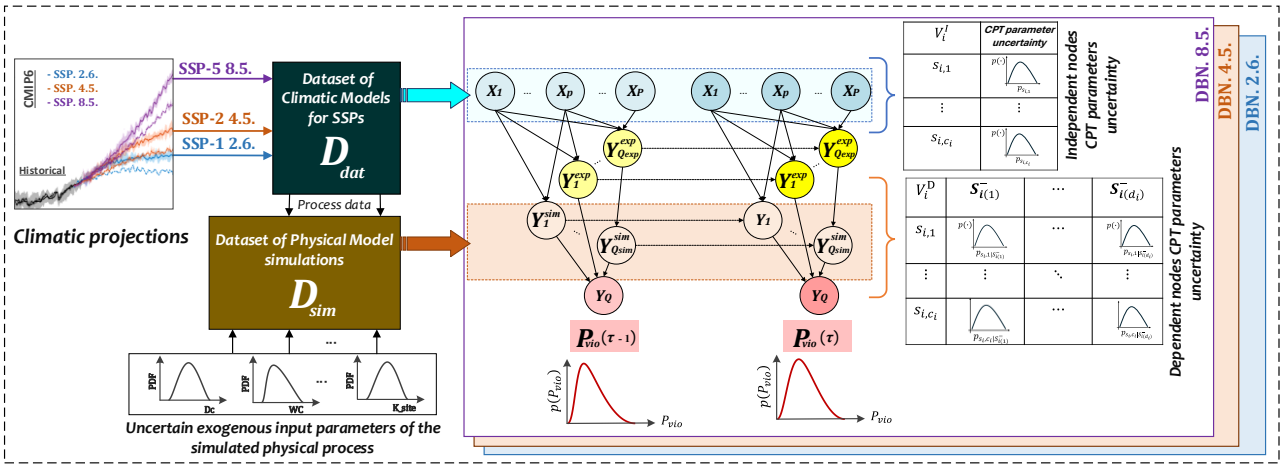


Fig. 2. DBN modeling to quantify the CPTs uncertainty of CC climatic nodes and FEPs simulation nodes, and propagate it through the DBN.

It is worth noting that CMIP6 projections are used in two distinct ways in the proposed modelling framework illustrated in Fig 2. For learning the CPTs of the CC nodes ($\mathbf{p}^{dat}$), the raw CMIP6 ensemble outputs are used directly (without preprocessing), so that inter-model spread is preserved and propagated as epistemic uncertainty. In contrast, Gaussian distributions are fitted to the CMIP6 ensemble only for MC sampling when generating $D_{sim}$, in order to provide stochastic CC inputs to the physics-based degradation models, without altering the CC node learning step. This innovative combined learning approach integrates $\boldsymbol{\mathcal{D}}_{sim}$, generated from physic-based models, with limited CC model dataset $\boldsymbol{\mathcal{D}}_{dat}$ to estimate the CPT parameters and their associated epistemic uncertainties.

Note that the CC climatic variables (temperature, relative humidity, and $CO_2$ concentration) are modeled as root nodes without explicit causal links among them. However, their statistical dependence is implicitly captured during CPT learning, as these variables are jointly sampled from the same CMIP6 climate model realizations for each SSP scenario and time slice. This approach preserves the correlation structure inherent in the climate projections and propagates it through the DBN at the parametric level.

In the following Section 2.1.1, we show how to quantify the uncertainty of $\mathbf{p}^{dat}$ and $\mathbf{p}^{sim}$ from $\boldsymbol{\mathcal{D}}_{dat}$ and $\boldsymbol{\mathcal{D}}_{sim}$ and, then, propagate this to estimate $\left[\underline{P_{vio}}(\tau), \overline{P_{vio}}(\tau)\right]_{\gamma}^{\beta}$.

### 2.1.1 CPTs parameters uncertainty quantification and propagation

To quantify the uncertainty of CPTs parameters of dependent nodes, Bayesian inference is used [54]: a Dirichlet prior distribution $\boldsymbol{p}_{s_i|\boldsymbol{s}_{i(m)}^-} \sim D\left(\alpha_{s_{i,1}|\boldsymbol{s}_{i(m)}^-}, \dots, \alpha_{s_{i,c_i}|\boldsymbol{s}_{i(m)}^-}\right)$ (i.e., a conjugate prior of the multinominal likelihood assumed for the data in $\boldsymbol{\mathcal{D}}_{dat}$ and $\boldsymbol{\mathcal{D}}_{sim}$) is assigned to the CPTs parameters:

$$p\left(p_{s_{i,1}|\boldsymbol{s}_{i(m)}^-}, \dots, p_{s_{i,c_i}|\boldsymbol{s}_{i(m)}^-} | \alpha_{s_{i,1}|\boldsymbol{s}_{i(m)}^-}, \dots, \alpha_{s_{i,c_i}|\boldsymbol{s}_{i(m)}^-}\right) = \frac{1}{\omega_{D|\boldsymbol{s}_{i(m)}^-}} \prod_{u=1}^{c_i} \left(p_{s_{i,u}|\boldsymbol{s}_{i(m)}^-}\right)^{\alpha_{s_{i,u}|\boldsymbol{s}_{i(m)}^-}-1} \tag{5}$$

where the normalization constant $\omega_{D|\boldsymbol{s}_{i(m)}^-}$ is equal to the integral over the simplex:

$$\omega_{D|\boldsymbol{s}_{i(m)}^-} = \int_{\Delta_{c_i-1}} \prod_{u=1}^{c_i} \left(p_{s_{i,u}|\boldsymbol{s}_{i(m)}^-}\right)^{\alpha_{s_{i,u}|\boldsymbol{s}_{i(m)}^-}-1} d\boldsymbol{p}_{s_i|\boldsymbol{s}_{i(m)}^-} \tag{6}$$

where $\Delta_{c_i-1} = \left\{\boldsymbol{p}_{s_i|\boldsymbol{s}_{i(m)}^-} \in \mathbb{R}^{c_i} | p_{s_{i,u}|\boldsymbol{s}_{i(m)}^-} \geq 0, \sum_u p_{s_{i,u}|\boldsymbol{s}_{i(m)}^-} = 1\right\}$.

The prior hyperparameters $\alpha_{s_{i,u}|\boldsymbol{s}_{i(m)}^-} > 0$ can be interpreted as pseudo-counts: each $\alpha_{s_{i,u}|\boldsymbol{s}_{i(m)}^-}$ reflects the number of times an expert expects to observe the event $\left(V_i = s_{i,u} \middle| \boldsymbol{V}_i^- = \boldsymbol{S}_{\boldsymbol{i}(m)}^-\right)$ in a hypothetical prior dataset. The prior distribution is, then, updated through Bayes theorem after observing the data in $\boldsymbol{\mathcal{D}}$ to compute the posterior $\boldsymbol{p}_{s_i|\boldsymbol{s}_{i(m)}^-}|\boldsymbol{\mathcal{D}} \sim D\left(\alpha_{s_{i,1}|\boldsymbol{s}_{i(m)}^-} + N_{s_{i,1}|\boldsymbol{s}_{i(m)}^-}, \dots, \alpha_{s_{i,c_i}|\boldsymbol{s}_{i(m)}^-} + N_{s_{i,c_i}|\boldsymbol{s}_{i(m)}^-}\right)$, where

$N_{s_{i,1}|\boldsymbol{s}_{i(m)}^-}, \dots, N_{s_{i,c_i}|\boldsymbol{s}_{i(m)}^-}$ are the numbers of times the events $\left(V_i = s_{i,1}\middle|\boldsymbol{V}_i^- = \boldsymbol{s}_{i(m)}^-\right), \dots, \left(V_i = s_{i,c_i}\middle|\boldsymbol{V}_i^- = \boldsymbol{s}_{i(m)}^-\right)$ are observed in $\boldsymbol{\mathcal{D}}$, respectively, and $N_{s_i|\boldsymbol{s}_{i(m)}^-} = \sum_u N_{s_{i,u}|\boldsymbol{s}_{i(m)}^-}$. Thus, the posterior mean and maximum a posteriori (MAP) estimates are given by [54]:

$$E\left[p_{s_{i,u}|\boldsymbol{s}_{i(m)}^-}|\boldsymbol{\mathcal{D}}\right] = \frac{\alpha_{s_{i,u}|\boldsymbol{s}_{i(m)}^-} + N_{s_{i,u}|\boldsymbol{s}_{i(m)}^-}}{\sum_{u=1}^{c_i} \alpha_{s_{i,u}|\boldsymbol{s}_{i(m)}^-} + N_{s_{i,u}|\boldsymbol{s}_{i(m)}^-}} \tag{7}$$

$$MAP(p_{s_{i,u}|\boldsymbol{s}_{i(m)}^-}|\boldsymbol{\mathcal{D}}) = \frac{\alpha_{s_{i,u}|\boldsymbol{s}_{i(m)}^-} + N_{s_{i,u}|\boldsymbol{s}_{i(m)}^-} - 1}{\sum_{u=1}^{c_i} \alpha_{s_{i,u}|\boldsymbol{s}_{i(m)}^-} + N_{s_{i,u}|\boldsymbol{s}_{i(m)}^-} - c_i} \tag{8}$$

The Bayesian updating proceeds analogously to Eqs. (5-8) for independent nodes, by removing the conditioning with respect to the combination of parent nodes combination $(\cdot)|\boldsymbol{S}_{\boldsymbol{i}(m)}^-$.

Note that whereas $p(\boldsymbol{p}_{s_i} \mid \mathcal{D}_{dat})$ *(*where $\boldsymbol{p}_{\boldsymbol{s_i}} \in \boldsymbol{p}^{dat}$*)* quantifies the (epistemic) climatic model uncertainty, $p(\boldsymbol{p}_{s_i|\boldsymbol{s}_{i(m)}^-}|\boldsymbol{\mathcal{D}})$ (where $\boldsymbol{p}_{s_i|\boldsymbol{s}_{i(m)}^-} \in \boldsymbol{p}^{sim}$ ) quantifies the epistemic uncertainty that arises from the incompleteness of physical model simulations. For a comprehensive on about how this latter affects the uncertainty of $\boldsymbol{p}^{sim}$, the interested reader may refer to [16].

When the total number of observed samples in $\boldsymbol{\mathcal{D}}$ is large (i.e., $\sum_{u=1}^{c_i} N_{s_{i,u}|\boldsymbol{s}_{i(m)}^-} \to \infty$), the type of prior becomes negligible on the posterior mean and MAP, i.e., both the posterior mean and MAP estimate converge to the MLE (i.e., $\hat{p}_{s_{i,u}|\boldsymbol{s}_{i(m)}^-}^{MLE} = \frac{N_{s_{i,u}|\boldsymbol{s}_{i(m)}^-}}{\sum_u N_{s_{i,u}|\boldsymbol{s}_{i(m)}^-}}$) reflecting a complete reliance on the observed data. Similarly, when $\sum_{u=1}^{c_i} \alpha_{s_{i,u}|\boldsymbol{s}_{i(m)}^-} \to 0$, the posterior mean converges to the MLE. However, a prior with any $\alpha_{s_{i,u}|\boldsymbol{s}_{i(m)}^-} = 0$ is improper (i.e., it does not integrate to a finite value), causing the posterior log-likelihood to diverge, if also $N_{s_{i,u}|\boldsymbol{s}_{i(m)}^-} = 0$. To avoid this, following [58], we employ a Bayesian Dirichlet–equivalent uniform (BDeu) uninformative prior by setting the hyperparameters of Eq. (5) as follows: $\alpha_{s_{i,u}|\boldsymbol{s}_{i(m)}^-} = \frac{\alpha}{c_i \cdot d_i}$ (dependent nodes), $\alpha_{s_{i,u}} = \frac{\alpha}{c_i}$ (independent nodes), where the equivalent sample size $\alpha$ (representing the total number of hypothetical prior observations) is defined as: $\alpha = \sum_u \sum_m \alpha_{s_{i,u}|\boldsymbol{s}_{i(m)}^-}$

(dependent nodes), $\alpha = \sum_u \alpha_{s_{i,u}}$ (for independent nodes). We set the equivalent sample size $\alpha = 1$ to ensure the posterior distribution is proper, thus avoiding divergence of the posterior log-likelihood when counts $N_{s_{i,u}|\boldsymbol{s}_{i(m)}^-}$ are zero. This choice minimizes the influence of the prior distribution while maintaining computational stability. For a detailed discussion on selecting the appropriate value of $\alpha$, the interested reader may refer to [58].

Once the DBN has been constructed and the uncertainty about $\mathbf{p}^{dat}$ and $\mathbf{p}^{sim}$ characterized via the posterior $\boldsymbol{p}_{s_i|\boldsymbol{s}_{i(m)}^-}|\boldsymbol{\mathcal{D}} \sim D\left(\alpha_{s_{i,1}|\boldsymbol{s}_{i(m)}^-} + N_{s_{i,1}|\boldsymbol{s}_{i(m)}^-}, \dots, \alpha_{s_{i,c_i}|\boldsymbol{s}_{i(m)}^-} + N_{s_{i,c_i}|\boldsymbol{s}_{i(m)}^-}\right)$ ($\boldsymbol{p}_{s_i}|\boldsymbol{\mathcal{D}} \sim D\left(\alpha_{s_{i,1}} + N_{s_{i,1}}, \dots, \alpha_{s_{i,c_i}} + N_{s_{i,c_i}}\right)$ for independent nodes) the uncertainty of the violation probability $P_{vio}$ can be represented using the non-parametric tolerance interval $\left[\underline{P_{vio}}(\tau), \overline{P_{vio}}(\tau)\right]_{\gamma}^{\beta}$, which characterizes its residual uncertainty, defined in this work as the uncertainty in the DBN output induced by propagating epistemic uncertainty in the CPT parameters (i.e., $\boldsymbol{p}^{dat}$ and $\boldsymbol{p}^{sim}$) through the network.

To determine $N_{\gamma}^{\beta}$, the required number of samples drawn from the (unknown) probability distribution $p\left(P_{vio}(\tau)\right)$, so that the interval $\left[\underline{P_{vio}}(\tau), \overline{P_{vio}}(\tau)\right]_{\gamma}^{\beta}$ covers at least a fraction $\gamma$ of the distribution with confidence $\beta$, we apply Wilks' formula [59]:

$$\beta = 1 - \gamma^{N_{\gamma}^{\beta}} - \left(N_{\gamma}^{\beta} - 1\right)(1-\gamma)\gamma^{N_{\gamma}^{\beta}-1} \tag{9}$$

where $\underline{P_{vio}}(\tau)$ and $\overline{P_{vio}}(\tau)$ denote the minimum and the maximum among the $N_{\gamma}^{\beta}$ sampled values from $p\left(P_{vio}(\tau)\right)$, respectively. To do that, the following algorithm is applied:

For $l = 1,2, \dots, N_{\gamma}^{\beta}$

i. Sample the CPTs parameters of CC climatic variables from $\boldsymbol{p}_{s_i}|\boldsymbol{\mathcal{D}}_{dat} \sim D\left(\alpha_{s_{i,1}} + N_{s_{i,1}}, \dots, \alpha_{s_{i,c_i}} + N_{s_{i,c_i}}\right)$ and update $\mathbf{p}^{dat}$ accordingly;

ii. Sample the CPTs parameters of $\bigcup_{\tau=0}^{\tau=T_\tau} \boldsymbol{Y^{sim}}(\tau)$ from $\boldsymbol{p}_{s_i|\boldsymbol{s}_{i(m)}^-}|\boldsymbol{\mathcal{D}}_{sim} \sim D\left(\alpha_{s_{i,1}|\boldsymbol{s}_{i(m)}^-} + N_{s_{i,1}|\boldsymbol{s}_{i(m)}^-}, \ldots, \alpha_{s_{i,c_i}|\boldsymbol{s}_{i(m)}^-} + N_{s_{i,c_i}|\boldsymbol{s}_{i(m)}^-}\right)$ and update $\mathbf{p}^{sim}$ accordingly;

iii. apply Eqs. (2-4) to compute $P_{vio}(\tau)_{(l)}$ for each $\tau = 0,1,\ldots,T_\tau$;

iv. Compute $\underline{P_{vio}}(\tau) = \min\left(P_{vio}(\tau)_{(1)}, \ldots, P_{vio}(\tau)_{\left(N_\gamma^\beta\right)}\right)$ and $\overline{P_{vio}}(\tau) = \max\left(P_{vio}(\tau)_{(1)}, \ldots, P_{vio}(\tau)_{\left(N_\gamma^\beta\right)}\right)$ for each $\tau = 0,1,\ldots,T_\tau$.

The pseudo-code for the estimation of $\left[\underline{P_{vio}}(\tau), \overline{P_{vio}}(\tau)\right]_\gamma^\beta$ is shown in Fig. 3.

**Algorithm 1:** $P_{vio}(\tau)$ tolerance interval computation

**Input** : $\mathcal{G}, \mathcal{D}_{dat}, \mathcal{D}_{sim}, \gamma, \beta$
**Output:** $[\underline{P}_{vio}(\tau), \overline{P}_{vio}(\tau)]$ for $\tau = 0, 1, \ldots, T_\tau$
Determine $N_\gamma^\beta$ from Wilks' formula (Eq. 9)
Set equivalent sample size $\alpha = 1$
Initialize $\vec{P}_{vio}^{samples}(\tau)$ for all $\tau$
**foreach** *CC node* $V_i \in \bigcup_{\tau=0}^{T_\tau} X(\tau)$ **do**
    Discretize continuous values in $\mathcal{D}_{dat}$
    Compute $N_{s_{i,u}} = \sum_{k=1}^{N_{dat}} \mathbb{1}(V_i(k) = s_{i,u})$
    Set $\alpha_{s_{i,u}} = \alpha / c_i$
**foreach** *FEP simulation node* $V_i \in \bigcup_{\tau=0}^{T_\tau} Y^{sim}(\tau)$ **do**
    Discretize continuous values in $\mathcal{D}_{sim}$
    **foreach** $\mathbf{S}_{i(m)}^- \in \mathbf{S}_i^-$ **do**
        Compute $N_{s_{i,u}|\mathbf{S}_{i(m)}^-}$
        Set $\alpha_{s_{i,u}|\mathbf{S}_{i(m)}^-} = \alpha / (c_i d_i)$
**foreach** $V_i \in \bigcup_{\tau=0}^{T_\tau} Y^{exp}(\tau)$ **do**
    Elicit and update the CPT in the DBN
**for** $l = 1$ **to** $N_\gamma^\beta$ **do**
    **foreach** $V_i \in \bigcup_{\tau=0}^{T_\tau} X(\tau)$ **do**
        Sample $\mathbf{p}_{s_i} \sim Dir(\alpha_{s_{i,*}} + N_{s_{i,*}})$
        Update the CPT
    **foreach** $V_i \in \bigcup_{\tau=0}^{T_\tau} Y^{sim}(\tau)$ **do**
        **foreach** $\mathbf{S}_{i(m)}^- \in \mathbf{S}_i^-$ **do**
            Sample $\mathbf{p}_{s_i|\mathbf{S}_{i(m)}^-}$
            Update the CPT
    **foreach** $\tau = 0, 1, \ldots, T_\tau$ **do**
        Compute $P_{vio}(\tau)_{(l)}$
        Store $P_{vio}(\tau)_{(l)}$ in $\vec{P}_{vio}^{samples}(\tau)$
**foreach** $\tau = 0, 1, \ldots, T_\tau$ **do**
    $\underline{P}_{vio}(\tau) = \min(\vec{P}_{vio}^{samples}(\tau))$
    $\overline{P}_{vio}(\tau) = \max(\vec{P}_{vio}^{samples}(\tau))$
**return** $[\underline{P}_{vio}(\tau), \overline{P}_{vio}(\tau)]$

Fig. 3. The pseudo-code for the estimation of $\left[\underline{P_{vio}}(\tau), \overline{P_{vio}}(\tau)\right]_\gamma^\beta$.

Key sources of deep uncertainty in climate variables are captured through two main mechanisms: (1) *scenario uncertainty* is addressed by developing separate DBNs for each SSP scenario (SSP-1 2.6, SSP-2 4.5, SSP-5 8.5); (2) *climatic model uncertainty* is captured through the CPT parameters $\boldsymbol{p}^{dat}$, where the spread among the projections from the $N_{dat} = 30$ available CMIP6 climate models determines the (epistemic) uncertainty of $\boldsymbol{p}^{dat}$. Specifically, Bayesian inference with Dirichlet prior distributions is employed to quantify this *climatic model uncertainty*, where the resulting posterior distributions $\mathbf{p}_{s_i} \mid \mathcal{D}_{dat} \sim D(\alpha_{s_{i,1}} + N_{s_{i,1}}, \dots, \alpha_{s_{i,c_i}} + N_{s_{i,c_i}})$ (for each $\boldsymbol{p}_{\boldsymbol{s_i}} \in \mathbf{p}^{dat}$) encode the degree of agreement (or disagreement) among climate models: larger spreads indicate greater model uncertainty, whereas closer posteriors reflect higher model agreement.

## 3. Case Study

We consider a near-surface NWR located in Dessel, Belgium [51], that is equipped with multiple engineering and natural barriers to prevent radionuclide migration. Specifically, the nuclear waste is encased within engineered concrete monoliths, then stacked within concrete modules situated on a sand-cement embankment at ground level. The entire structure is eventually covered with an additional upper concrete, limited by the upper natural soil barrier and the natural barriers, which include the unsaturated soil zone and the underlying aquifer, both contributing to the passive attenuation of radionuclide transport through physical, chemical and hydrological processes. The Dessel NWR has been selected as a reference case study because it has been extensively analyzed in previous PA studies [16] and detailed information is available in literature [60]. It is important to emphasize that the objective of this case study is methodological rather than site-specific, i.e., this aimed to propose a method to account for CC deep uncertainty in long-term PA. The proposed modelling framework is, therefore, site-independent and can be extended to other NWRs by adapting site-specific climatic scenarios, material, and environmental data.

We adopt a conservative infiltration scenario in which the natural barriers are excluded, i.e., soil barrier, unsaturated zone and aquifer are not considered here [16], so that the surface water is assumed to directly

penetrate the top cover roof of the repository, seeps through the engineering concrete barriers and initiates the leaching of radionuclides. The radionuclides could harm humans through the consumption of water from wells located downstream of the repositories; it is also conservatively assumed that household water consumption is contaminated from such a well. To capture long-term concrete degradation under CC variables projections, two chemical degradation processes of the concrete engineering barriers are modeled as explicitly time-dependent FEPs: carbonation-induced corrosion and chloride ingress. These two degradation mechanisms are selected based on experimental evidence and prior studies that identified them as the dominant climate-driven degradation processes affecting concrete barriers in NWRs [61, 62], with temperature and relative humidity identified as the main climatic drivers influencing their progression [63].

The proposed DBN (Fig. 4) is modelled in the GeNIe/SMILE package [64], and is built on a discrete set of nine time slices, $\tau = 0,1, \dots ,8$, of time step $\Delta t = 10\ yr$, spanning from 2020 ($\tau = 0$) to 2100 ($\tau = 8$). This decadal temporal resolution allows capturing the gradual evolution of both CC variables and concrete degradation processes, since CC variables projections uncertainties become dominant at decadal scales [46], and concrete chemical degradation processes become relevant over years to decades [10, 65]. This ensures sufficient granularity to observe the transition of carbonation and chloride ingress states from safe to unsafe conditions over the assessment period (see Fig. 5). With $P = 3$ CC variables, $Q_{sim} = 2$ simulated FEPs, $Q_{exp} = 8$ expert-based FEPs, the total number of DBN nodes is $n_{tot} = \left(P + Q_{sim} + Q_{exp}\right) \cdot (T_\tau + 1) = 13 \times 9 = 117$. The DBN nodes are briefly summarized as follows:

- CC climatic variables $\boldsymbol{X}(\tau) = \{X_T(\tau), X_{RH}(\tau), X_{CO_2}(\tau)\}$: temperature, relative humidity and atmospheric $CO_2$ concentration (blue nodes in Fig. 4);
- Simulated FEPs $\boldsymbol{Y}^{sim}(\tau) = \{Y_C(\tau), Y_{Cl}(\tau)\}$: carbonation and chloride ingress processes simulated with the physics-based models of Appendix A (orange nodes in Fig. 4), which are influenced by CC variables determining the chemical degradation state of $V_{CD}(\tau)$, Carbonation $V_C(\tau)$ and chloride ingress $V_{Cl}(\tau)$ nodes are modeled as two independent degradation phenomena, and their combined

effect on the concrete barrier is captured in the *Chemical Degradation* node $V_{CD}(\tau)$ through a logical OR connection, indicating that the degradation occurs when either one or both exceed their respective critical thresholds [17]. This corresponds to $P_C \cap P_{Cl} \neq \emptyset$, i.e., at least one of the two degradation mechanisms exceeds its threshold (logical OR) as summarized in Table 1;

- Expert-based FEPs $\boldsymbol{Y}^{exp}(\tau)$: Earthquake, monolith mechanical degradation, crack aperture, hydraulic conductivity, water flux, diffusion coefficient and distribution coefficient, whose CPTs are taken from [60] (yellow nodes in Fig. 4);
- Safety target $Y_Q(\tau) = \{V_{DI}(\tau)\}$ : Dose intake violation, i.e., $P_{vio}(\tau) = \Pr(DI(\tau) > 1\,{}^{mSv}/_{yr})$, (red nodes in Fig. 4).

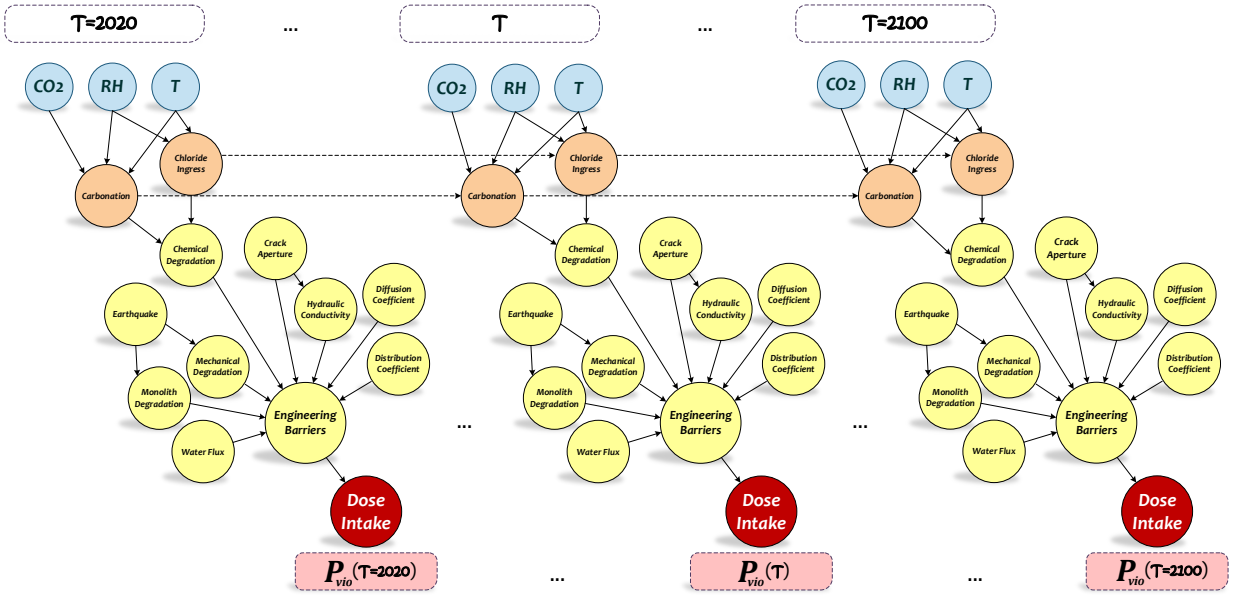


Fig. 4. DBN for the near-surface NWR case study [16].

The proposed DBN structure (Fig. 4) is built with reference to that proposed in [16, 51] for the same case study, which is here expanded to encode the causal relationships between CC variables and concrete degradation processes, as suggested in [10, 65-67]. Specifically, the novel structure includes: (i) *intra-slice* edges to model the direct influence of climatic variables (blue nodes) on the chemical degradation

FEPs (orange nodes), based on the physics of carbonation and chloride ingress processes (see Appendix A); (ii) *intra-slice* edges to model the interdependencies among FEPs (orange nodes, for the chemical degradation FEPs, and yellow nodes for all the other FEPs) and their effects on the safety target (dose intake, red node) within the same time slice, as already described in [16]; (iii) *inter-slice* edges to model the cumulative nature of carbonation and chloride penetration, specifically, $V_C(\tau) \rightarrow V_C(\tau+1)$ and $V_{Cl}(\tau) \rightarrow V_{Cl}(\tau+1)$.

The CC climatic nodes and simulated nodes are discretized into the states listed in Table 1, whereas the expert-based nodes are kept the same as in [49]. The discretization thresholds for degradation-related variables are defined based on critical limits reported in the literature for carbonation-induced corrosion [67] and chloride ingress [65], whereas thresholds for CC variables are derived from the empirical quantile structure of the CMIP6 ensemble.

Table 1. States definition of climatic and simulation nodes of Fig. 4, derived from continuous ranges.

| ID | Node Description | States | | | Ranges | | |
|---|---|---|---|---|---|---|---|
| $V_T$ | Temperature ($K$) | Low | Medium | High | [0, 285) | [285, 287) | [287, +∞] |
| $V_{RH}$ | Relative humidity (%) | Mild | Normal | Humid | [0, 0.7) | [0.7, 0.8) | [0.8, 1] |
| $V_{CO_2}$ | $CO_2$ Concentration ($ppm$) | Low500 | High500 | | [0, 500) | [500, +∞] | |
| $V_C$ | Carbonation ($cm$) | Safe | Unsafe ($P_C$) | | [0, 3) | [3, +∞] | |
| $V_{Cl}$ | Chloride ingress ($\frac{kg}{m^3}$) | Uncritical | Critical ($P_{Cl}$) | | [0, 0.9) | [0.9, +∞] | |
| $V_{CD}$ | Chemical Degradation (CD) | Without CD | With CD | | $P_C \cap P_{Cl} = \emptyset$ | $P_C \cap P_{Cl} \neq \emptyset$ | |

For learning the CPTs, two datasets are used:

- CC dataset ($\boldsymbol{\mathcal{D}}_{dat}$): CMIP6 ensemble projections for Belgium (where the considered NWR is located) under three SSPs (SSP-1 2.6, SSP-2 4.5, SSP-5 8.5). For each SSP and time slice, the $N_{dat} = 30$ available climatic models deliver the CC variables $\boldsymbol{X}(\tau) = \{X_T(\tau), X_{RH}(\tau), X_{CO_2}(\tau)\}$.
- Simulation dataset ($\boldsymbol{\mathcal{D}}_{sim}$): $N_{sim} = 10^4$ Monte-Carlo simulations of the carbonation-induced and chloride-ingress models per SSP and time slice, performed by sampling the uncertain exogenous model parameters from the distributions of Table 2 (derived from experimentally validated physics-based models and supporting experimental studies [10]; see Appendix A), and the CC

variables relevant for corrosion models from the Tables 3-4 (i.e., normal (Gaussian) distributions fitted to the ensemble of available models for the CC variable at each $\tau$ and SSP scenario, which are used to generate $N_{sim}$ samples that drive the carbonation and chloride ingress simulations and, in turn, the learning of the corresponding CPTs). The outputs of carbonation depth and Chloride concentration values (as provided in Appendix A) are, then, discretized according to Table 1.

All the other nodes CPTs (*Earthquake*, *Monolith Degradation*, *Mechanical Degradation*, *Water Flux*, *Crack Aperture*, *Hydraulic Conductivity*, *Diffusion Coefficient*, and *Distribution Coefficient*), i.e., $\forall\, Y_q^{exp}(\tau) \in \boldsymbol{Y^{exp}}(\tau)$ are kept as provided in [60]. These CPTs are derived from a multi-physics reactive–transport modelling framework that accounts for interacting degradation mechanisms, including coupled physical processes (e.g., mechanical damage and transport properties) and chemical processes (e.g., diffusion and sorption) [16, 62]. These conditional dependencies between degradation mechanisms, encoded in the CPTs, allow their combined influence to propagate to the dose intake violation state.

Temporal consistency in DBN parameter learning is ensured through: (i) a time-homogeneous transition structure, where inter-slice dependencies (e.g., $V_C(\tau) \rightarrow V_C(\tau+1)$) maintain consistent conditional relationships across all time slices; (ii) physics-based constrains: CPT parameters for the simulated FEPs (i.e., $\bigcup_{\tau=0}^{\tau=T_\tau} \boldsymbol{Y^{sim}}(\tau)$) are learned from a dataset generated by physical models that inherently capture temporal dynamics through aging factors and time-dependent diffusion coefficients (see Appendix A); (iii) consistent state discretization (Table 1) across all time slices.

Table 2. Distributions of the uncertain exogenous parameters of the carbonation and chloride ingress models.

| Parameter | Symbol | Unit | Distribution | Mean | COV | Ref. |
|---|---|---|---|---|---|---|
| Initial carbon dioxide ($CO_2$) diffusion coefficient obtained at $t_0$ | $D_C$ | $\frac{cm^2}{s}$ | Normal | 2.22e-4 | $\sigma = 0.15$ | [65] |
| Aging factor | $n_d$ | - | Normal | 0.24 | 0.12 | [65-67] |
| Factor for exposure microclimatic wetting ang drying cycles (for unsheltered outdoor) | $n_m$ | - | Normal | 0.12 | 0. 1 | - |

| | | | | | | |
|---|---|---|---|---|---|---|
| Cement content | $C_e$ | $\frac{kg}{m^3}$ | Normal | 300 | 0.1 | [68] |
| Calcium oxide ($C_aO$ ) content in the cement | $C_aO$ | - | Uniform | 0.65 | 0.1 | - |
| Water to cement ratio | $^{w}/_{c}$ | - | Lognormal | 0.5 | 0.05 | [69-71] |
| Diffusion coefficient of chloride ions in dry concrete | $D_{Cl}$ | $\frac{m^2}{s}$ | Lognormal | 6.0e-12 | 0.2 | [72] |
| Initial chloride concentration at the surface | $C_0^{Cl}$ | $\frac{kg}{m^3}$ | Normal | 1.15 | 0.5 | [72] |
| Factor for potential increase of $CO_2$ concentration in industrial area | $k_{site}$ | - | Normal | 1.15 | 0.1 | [65] |
| Environmental factor | $k_e$ | - | Gamma | 0.924 | $\sigma = 0.155$ | [70] |
| Test corrosion factor | $k_t$ | - | Normal | 0.832 | $\sigma = 0.024$ | [70] |
| Cutting time corrosion factor | $k_c$ | - | Beta | 2.4 | $\sigma = 0.7$ | [70] |
| Activation energy | $E$ | $\frac{KJ}{mol}$ | Uniform | 38.3 | 0.09 | [68] |

Table 3. Statistical process values of annual mean temperature for Belgium during 2020-2100 based on CMPI6.

| **Climatic projections** | | **Timing slices ($\tau$)** | | | | | | | |
|---|---|---|---|---|---|---|---|---|---|
| | | 2030 | 2040 | 2050 | 2060 | 2070 | 2080 | 2090 | 2100 |
| *SSP-1 2.6.* | Mean | 284.25 | 284.24 | 284.54 | 284.71 | 284.73 | 285.05 | 284.86 | 284.7 |
| | COV | 0.0036 | 0.0037 | 0.0039 | 0.0041 | 0.0041 | 0.0046 | 0.0050 | 0.0052 |
| *SSP-2 4.5.* | Mean | 284.27 | 284.68 | 284.87 | 285.12 | 285.28 | 285.49 | 285.78 | 286.03 |
| | COV | 0.0039 | 0.0035 | 0.0040 | 0.0039 | 0.0041 | 0.0040 | 0.0044 | 0.0043 |
| *SSP-5 8.5.* | Mean | 284.37 | 284.99 | 285.42 | 285.93 | 286.58 | 287.41 | 288.17 | 288.94 |
| | COV | 0.0043 | 0.0041 | 0.0042 | 0.0044 | 0.0045 | 0.0050 | 0.0052 | 0.0055 |

Table 4. Statistical estimated values of relative humidity change for Belgium during 2020-2100 based on CMPI6.

| **Climatic projections** | | **Timing slices ($\tau$)** | | | | | | | |
|---|---|---|---|---|---|---|---|---|---|
| | | 2030 | 2040 | 2050 | 2060 | 2070 | 2080 | 2090 | 2100 |
| *SSP-1 2.6.* | Mean | 9.52 | 10.07 | 11.66 | 12.71 | 12.47 | 14.18 | 14.16 | 13.43 |
| | COV | 0.5477 | 0.5648 | 0.5631 | 0.5222 | 0.5468 | 0.5325 | 0.5741 | 0.6688 |
| *SSP-2 4.5.* | Mean | 9.18 | 11.99 | 13.43 | 14.99 | 16.030 | 17.14 | 17.86 | 19.64 |
| | COV | 0.5911 | 0.5526 | 0.4949 | 0.4939 | 0.5080 | 0.4606 | 0.4624 | 0.4405 |
| *SSP-5 8.5.* | Mean | 11.08 | 14.41 | 16.62 | 19.07 | 23.01 | 29.54 | 32.80 | 38.47 |
| | COV | 0.5279 | 0.4915 | 0.4051 | 0.3811 | 0.3881 | 0.3855 | 0.3771 | 0.3732 |

To intuitively show the SSPs scenario uncertainty effect on carbonation and chloride ingress, their depths are estimated at each $\tau$ using the carbonation and chloride-induced corrosion models described in Appendix A, respectively. Results are plotted in Fig. 5, when the parameters of the carbonation-induced and chloride ingress degradation models are at their mean value as provided in Table 2, and the uncertainty related with the CC-variables projections is neglected (the mean values of the CC-variables at each $\tau$ are used, as provided in Tables 3-4). It can be seen that, due to a significant increase of $CO_2$ in all

SSPs, the carbonation (left) exceeds the critical depth (set to 3 $cm$ [67]) at 2072, 2076 and 2080 for SSP-5 8.5, SSP-2 4.5 and SSP-1 2.6, respectively; whereas the Chloride ingress critical depth (right), defined as the depth at which the chloride concentration exceeds $0.9\frac{kg}{m^3}$, assuming a surface chloride concentration of $1.15\frac{kg}{m^3}$ [65], increases with time (for example, under SSP-5 8.5, it exceeds 4.5 $cm$ in 2090). The profiles of carbonation depth and chloride ingress under different SSP scenarios, plotted in Fig. 5, are necessary to calculate the quantitative performance metrics of the NWR, specifically time-dependent exceedance probabilities of the degradation thresholds for carbonation depth and critical chloride concentration, are calculated in Section 4 (Figs. 6–7), and they are propagated through the DBN, to compute the dose-intake violation probability $P_{\text{vio}}(\tau)$ (Fig. 8), that is the primary quantitative safety metric used in the long-term PA of NWRs.

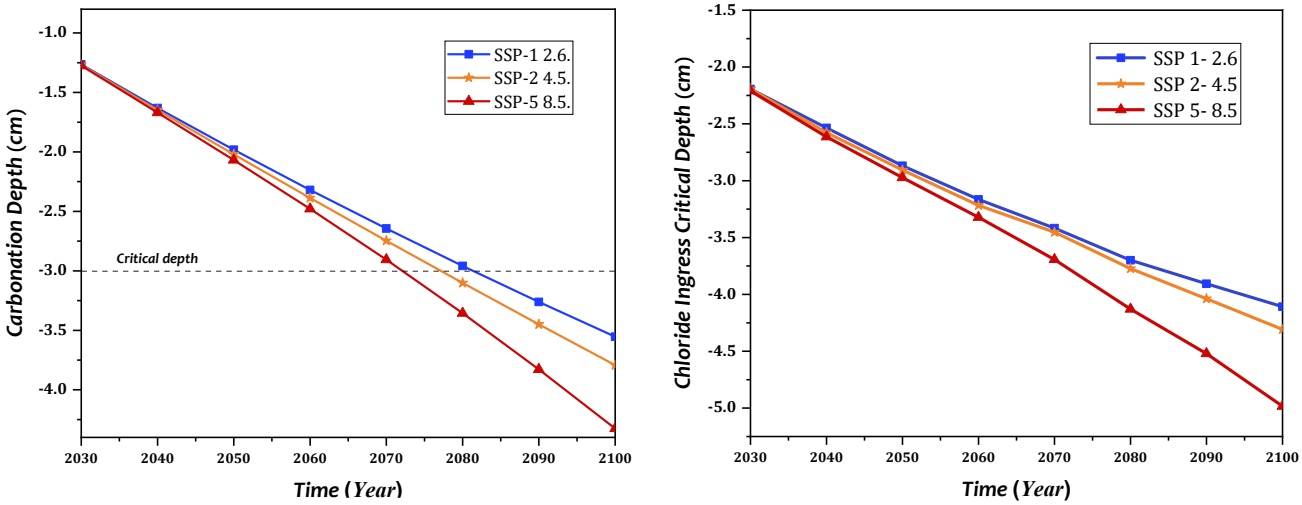


Fig. 5. Time-dependent corrosion depths of (left) carbonation and (right) chloride ingress, considering the impacts of temperature and relative humidity for Belgium during climatic projections for 2030-2100.

Following Section 2.1.1, we quantify the residual uncertainty associated with the following probabilities:

- Carbonation exceedance probability $P_C(\tau) = \Pr(V_C(\tau) = Unsafe)$, defined as the probability that the carbonation depth exceeds the safety threshold of 3 $cm$;
- Chloride ingress exceedance probability $P_{Cl}(\tau) = \Pr(V_{Cl}(\tau) = Critical)$, defined as the probability that the chloride ingress exceeds the safety threshold of $0.9\frac{kg}{m^3}$;

- Dose intake violation probability $P_{vio}(\tau) = \Pr(V_{DI}(\tau) > 1\frac{mSv}{yr})$, defined as the probability of exceeding an annual dose intake of 1 mSv/year.

We estimate these uncertainties using non-parametric tolerance intervals: $\left[\underline{P_C}(\tau), \overline{P_C}(\tau)\right]_{\gamma}^{\beta}$ for carbonation exceedance probability, $\left[\underline{P_{Cl}}(\tau), \overline{P_{Cl}}(\tau)\right]_{\gamma}^{\beta}$ for chloride ingress exceedance probability and $\left[\underline{P_{vio}}(\tau), \overline{P_{vio}}(\tau)\right]_{\gamma}^{\beta}$ for dose intake violation probability, with tolerance levels set at $\gamma = 0.95$ and confidence level $\beta = 0.95$, resulting in a sample size requirement of $N_{\gamma}^{\beta} = 93$ [73].

The computational complexity of exact inference in Bayesian networks is known to be NP-hard in general and to scale exponentially with the treewidth of the network (which is a measure of the size of the largest variable clusters that arise during inference) [50, 74]. However, some characteristics of the proposed DBN ensure tractable inference: first, the network structure exhibits sparse connectivity: inter-slice dependencies are limited to two temporal edges per time step (i.e., $V_C(\tau) \rightarrow V_C(\tau + 1)$ and $V_{Cl}(\tau) \rightarrow V_{Cl}(\tau + 1)$), which maintains a bounded treewidth throughout the unrolled network. Second, the discrete state space is compact, with most nodes having only two to three states (Table 1), thereby limiting the size of the CPTs. Under these conditions, a single complete inference pass through the 117-node DBN requires approximately 0.5 seconds on a standard workstation (Intel Core i7, 8 GB RAM). The tolerance interval estimation procedure, which requires $N_{\gamma}^{\beta} = 93$ DBN evaluations per SSP scenario, completes in under one minute per scenario. Thus, the proposed framework remains computationally feasible for the PA time horizons considered in this study. Incorporating additional FEPs can increase the network treewidth and, consequently, the computational burden. In such cases, approximate BN inference algorithms [54] may be required to achieve scalability.

## 4. Results and Discussion

Fig. 6 shows the tolerance interval $\left[\underline{P_C}(\tau), \overline{P_C}(\tau)\right]_{\gamma}^{\beta}$ (blue solid line) determined by the $N_{\gamma}^{\beta} = 93$ realizations of $P_C(\tau)$ (cloud of blue points), i.e., $\underline{P_C}(\tau) = \min\left(P_C(\tau)_{(1)}, \dots, P_C(\tau)_{\left(N_{\gamma}^{\beta}\right)}\right)$ and $\overline{P_C}(\tau) = \max\left(P_C(\tau)_{(1)}, \dots, P_C(\tau)_{\left(N_{\gamma}^{\beta}\right)}\right)$, computed for scenarios SSP-1 2.6, SSP-2 4.5, and SSP-5 8.5. To verify that the proposed framework produces realistic predictions, in Fig. 6, we compare $\left[\underline{P_C}(\tau), \overline{P_C}(\tau)\right]_{\gamma}^{\beta}$ against the Monte Carlo estimate of the carbonation exceedance probability $\hat{P}_{MC}^{C}(\tau)$, which is obtained, for each SSP scenario, simulating $N_{MC} = 10^6$ times the carbonation-induced corrosion model (Eq. A.1) by sampling the uncertain input parameters from the distributions specified in Tables 2–4. Correspondingly, the black square indicates the point estimate $\hat{P}_{MLE}^{C}$ obtained using the MLE of $\mathbf{p}^{dat}$ and $\mathbf{p}^{sim}$ (i.e., the standard approach of literature for learning CPTs parameters).

The accuracy of predictions is customarily quantified by K-fold cross-validation (e.g., 10-fold CV) when independent experimental or simulated data with known ground truth are available [75, 76]. In our context of DBN-based PA of NWRs, such data is not available, for example, for the CPT parameters of earthquake, monolith degradation, crack aperture, hydraulic conductivity, chemical degradation, engineering barriers and dose intake nodes (i.e., $\boldsymbol{Y}^{\boldsymbol{exp}}(\tau)$). Without ground truth values, cross-validation would not yield a meaningful estimate of predictive performance. Instead, we compare the proposed RIC method against an alternative approach that employs bootstrap for the estimation of CPT parameters uncertainty. Specifically, we compare $\left[\underline{P_C}(\tau), \overline{P_C}(\tau)\right]_{\gamma}^{\beta}$ against the bootstrap-based tolerance interval $\left[\underline{P_C^{boot}}(\tau), \overline{P_C^{boot}}(\tau)\right]_{\gamma}^{\beta}$ (green solid line in Fig. 6), where $\underline{P_C^{boot}}(\tau)$ and $\overline{P_C^{boot}}(\tau)$ denote the lower and upper bounds, respectively. In the bootstrap-based approach: (i) the learning datasets $\boldsymbol{\mathcal{D}}_{dat}$ and $\boldsymbol{\mathcal{D}}_{sim}$ are resampled with replacement $B = N_{\gamma}^{\beta}$ times, preserving their dimensionality; (ii) for each bootstrap replicate $b = 1, \dots, B$, the corresponding MLE of the CPTs parameter sets $\boldsymbol{p}^{dat,(b)}$ and $\boldsymbol{p}^{sim,(b)}$ are

estimated and (iii) the probability $P_C^{(b)}(\tau)$ is computed via DBN inference (Eq. 4). The bootstrap tolerance interval is, then, obtained by taking the minimum and maximum of the empirical sample $\left\{P_C^{(b)}(\tau)\right\}_{b=1}^{B}$, ensuring coverage $\gamma$ and confidence $\beta$, according to Wilks' formula [59].

Fig. 7 and Fig. 8 show the same statistics as Fig. 6 for $P_{Cl}(\tau)$ and $P_{vio}(\tau)$, respectively. However, it is worth pointing out that no Monte Carlo estimate is provided in Fig. 8 for $P_{vio}(\tau)$: whereas $\hat{P}_{MC}^{C}$ and $\hat{P}_{MC}^{Cl}$ are computed by directly simulating the physics-based degradation models (Appendix A), thereby providing a validation of the DBN-based estimates against the underlying physical processes, the dose intake node $V_{DI}(\tau)$ not only depends on the simulated degradation FEPs but also on several expert-elicited FEPs (e.g., earthquake, monolith degradation, crack aperture, hydraulic conductivity), for which no equivalent physical simulation model is available, not allowing the reliance on a direct Monte Carlo benchmark for $P_{vio}(\tau)$. Thus, the DBN inference remains the primary means of estimating $P_{vio}(\tau)$.

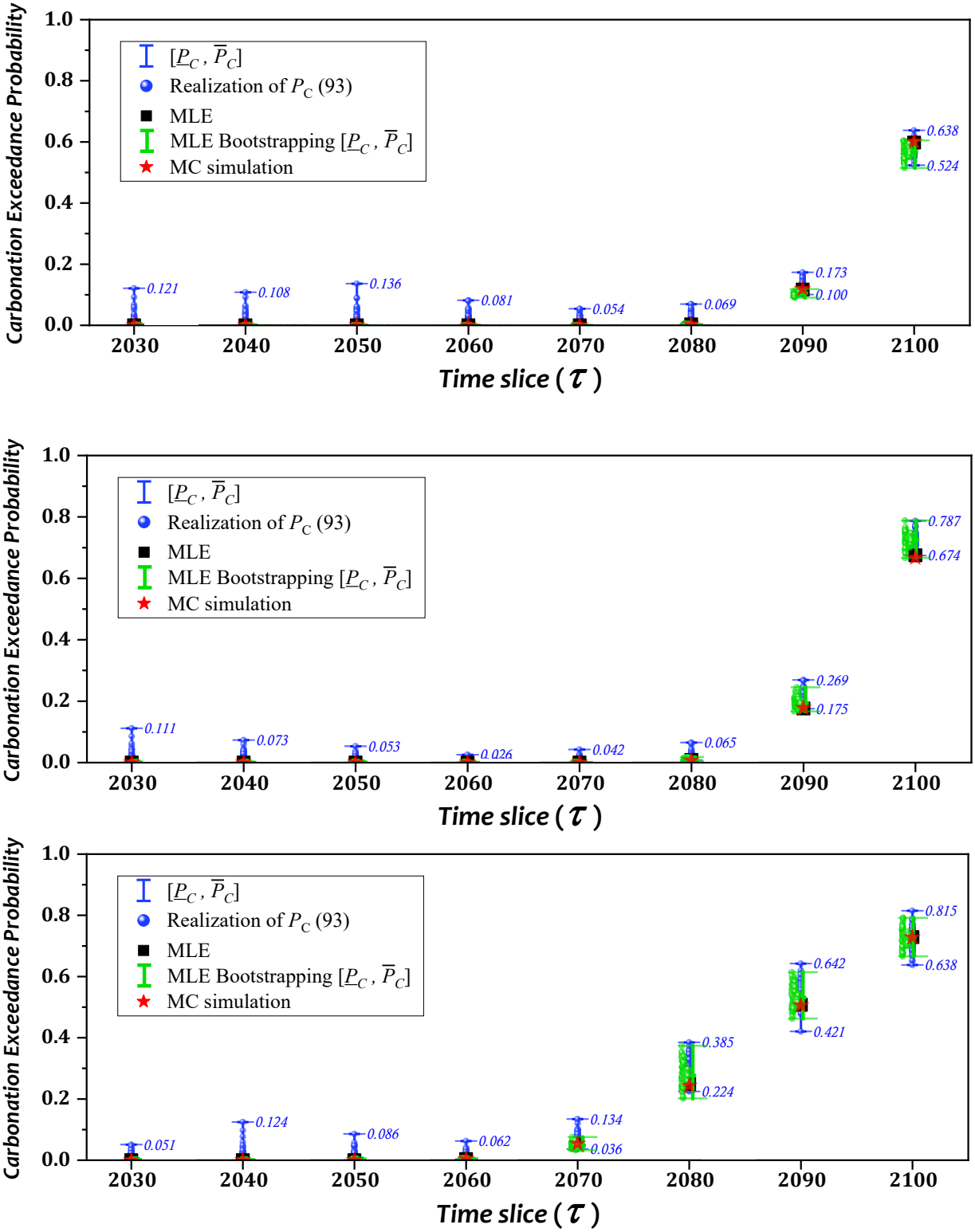


Fig. 6. Residual uncertainty for carbonation exceedance probabilities during time slices from 2030 to 2100, for SSP-1 2.6 (above), SSP-2 4.5 (center), SSP-5 8.5 (below).

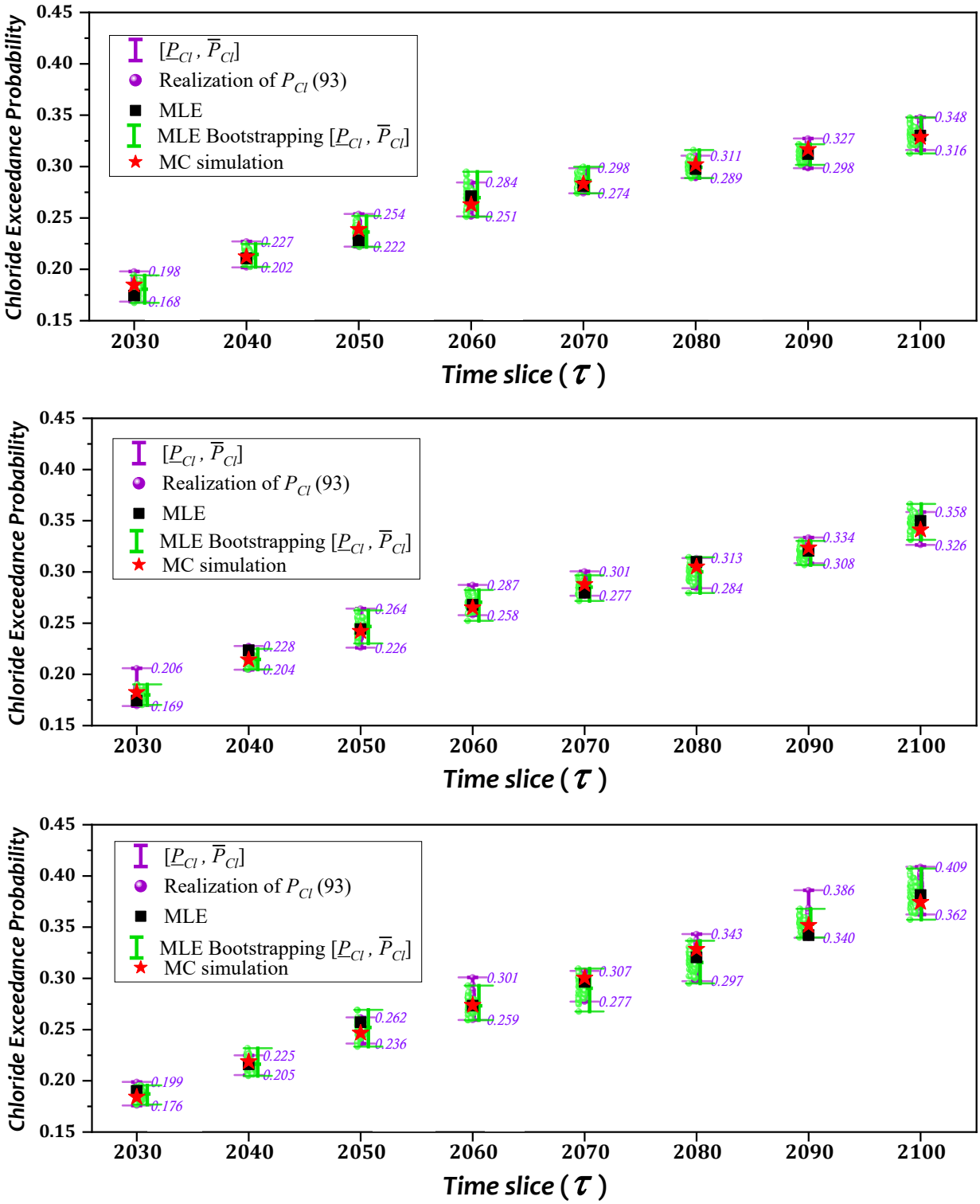


Fig. 7. Residual uncertainty for chloride ingress exceedance probabilities during time slices from 2030 to 2100, for SSP-1 2.6 (above), SSP-2 4.5 (center), SSP-5 8.5 (below).

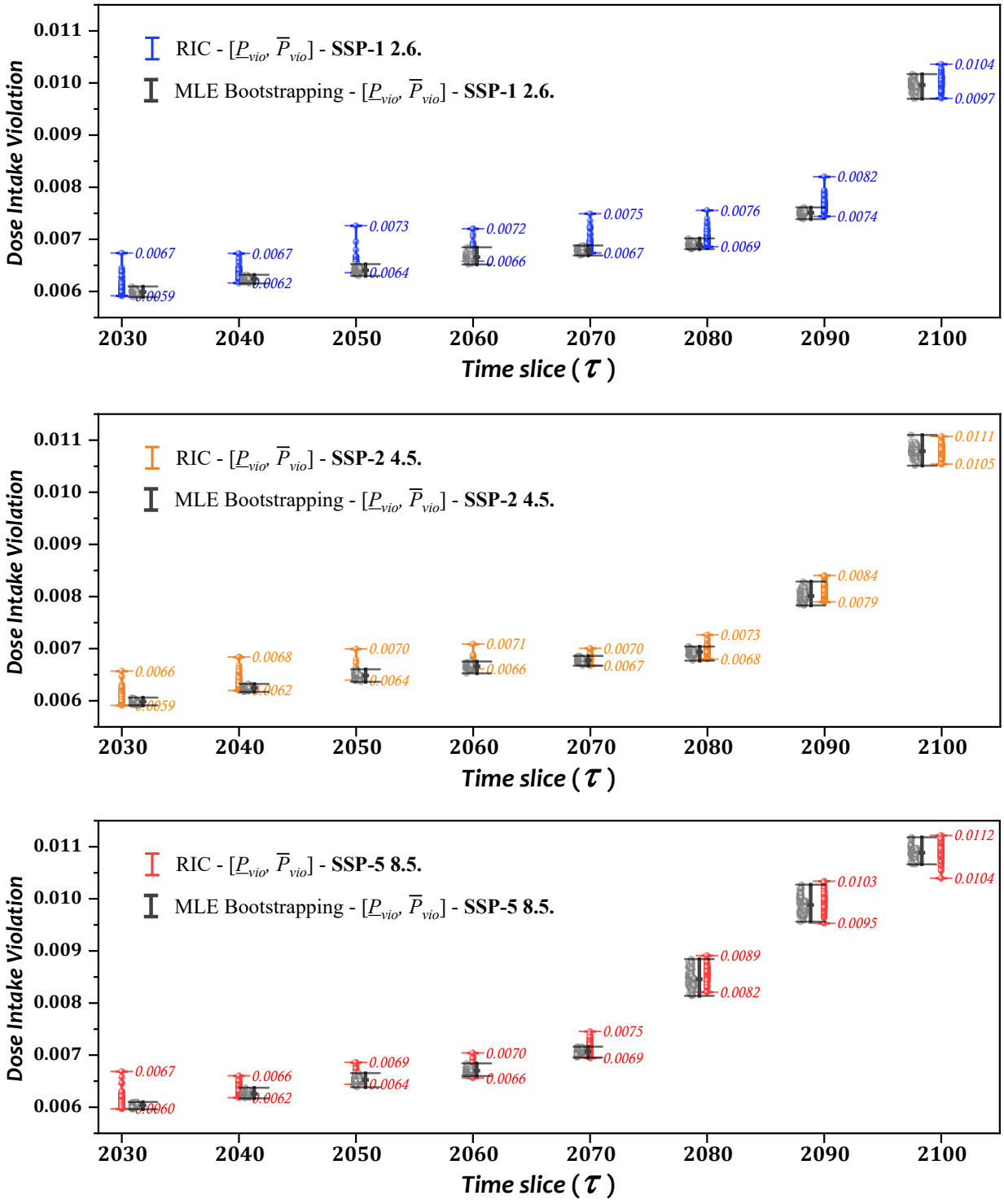


Fig. 8. Residual uncertainty for dose intake violation probabilities during time slices from 2030 to 2100, for SSP-1 2.6 (above), SSP-2 4.5 (center), SSP-5 8.5 (below).

As shown in Fig. 6 and Fig. 7, the MC estimates $\hat{P}_{MC}^{C}$ and $\hat{P}_{MC}^{Cl}$ (red stars) consistently fall within the tolerance intervals $\left[\underline{P_C}(\tau), \overline{P_C}(\tau)\right]_{\gamma}^{\beta}$ and $\left[\underline{P_{Cl}}(\tau), \overline{P_{Cl}}(\tau)\right]_{\gamma}^{\beta}$, respectively, across all time slices and SSP scenarios. This demonstrates that the DBN framework captures the essential behavior of the underlying physical processes, bounding the uncertainty stemming from limited climate model data and simulation variability. Furthermore, the MLE-based point estimates ($\hat{P}_{MLE}^{C}$ and $\hat{P}_{MLE}^{Cl}$) are in close agreement with the MC estimates, confirming that the CPT learning procedure preserves the statistical properties of the physical models. The broad tolerance intervals (e.g., $\overline{P_C}(\tau = 2090) - \underline{P_C}(\tau = 2090) \cong 0.22$, for SSP-5 8.5) highlight the significant residual uncertainty in the carbonation and chloride corrosion exceedance probability, that might have been overlooked, otherwise: incorporating such deep uncertainty related to CC enhances the PA of NWR, providing a conservative (yet trustworthy) assessment of the phenomena occurring, well-suited for decision making in the presence of deep uncertainty. Indeed, since the upper bounds $\overline{P_C}(\tau)$ and $\overline{P_{Cl}}(\tau)$ exceed $\hat{P}_{MLE}^{C}$ and $\hat{P}_{MLE}^{Cl}$, neglecting the deep uncertainty of CC variables may lead to underestimating the probability of chemical degradation from carbonation and chloride ingress.

Note that while for $P_C(\tau)$ the bootstrap-based tolerance interval always lies within the interval computed using the proposed RIC method (i.e., $\left[\underline{P_C^{boot}}(\tau), \overline{P_C^{boot}}(\tau)\right]_{\gamma}^{\beta} \subseteq \left[\underline{P_C}(\tau), \overline{P_C}(\tau)\right]_{\gamma}^{\beta}$ for each $\tau = 0, \dots, T_\tau$) (Fig. 6), this does not always hold for $P_{Cl}(\tau)$ (i.e., $\left[\underline{P_{Cl}^{boot}}(\tau), \overline{P_{Cl}^{boot}}(\tau)\right]_{\gamma}^{\beta} \not\subseteq \left[\underline{P_{Cl}}(\tau), \overline{P_{Cl}}(\tau)\right]_{\gamma}^{\beta}$) (Fig. 7). The difference arises from the fundamentally different ways in which the proposed RIC method and the bootstrap-based method treat conditional probabilities $p_{s_{i,u}|\boldsymbol{s}_{i(m)}^{-}}$ in the presence of unobserved parent state combinations (i.e., when $\sum_{u=1}^{c_i} N_{s_{i,u}|\boldsymbol{s}_{i(m)}^{-}} = 0$). In such cases, the MLE $\hat{p}_{s_{i,u}|\boldsymbol{s}_{i(m)}^{-}}^{MLE} = \frac{N_{s_{i,u}|\boldsymbol{s}_{i(m)}^{-}}}{\sum_u N_{s_{i,u}|\boldsymbol{s}_{i(m)}^{-}}}$ is undefined. Then, the bootstrap-based approach handles this situation by assigning fixed probabilities $p_{s_{i,u}|\boldsymbol{s}_{i(m)}^{-}}^{(b)} = 1/c_i$ for $u = 1, \dots, c_i$. Since this assignment is identical across all bootstrap resamples (because the parent-state combination remains unobserved in every resample), the resulting bootstrap

distribution exhibits zero variance for these parameters, thus failing to represent the epistemic uncertainty associated with data scarcity. In contrast, the RIC method samples $p_{s_{i,u}|\boldsymbol{s}_{i(m)}^{-}}$ from the Dirichlet posterior $Dir\left(\alpha_{s_{i,1}|\boldsymbol{s}_{i(m)}^{-}}, \ldots, \alpha_{s_{i,c_i}|\boldsymbol{s}_{i(m)}^{-}}\right)$ which, despite having the same expected value as the bootstrap estimate (i.e., given the BDeu prior, $E\left[p_{s_{i,u}|\boldsymbol{s}_{i(m)}^{-}}\right] = 1/c_i$), exhibits significant variance. This variance explicitly represents the epistemic uncertainty associated with unobserved parent state combinations and is propagated through the DBN inference. Table 4 reports, for $V_C$ and $V_{Cl}$, the number of unobserved parent state combinations (i.e., how many of the $d_i$ parent state combinations in $\boldsymbol{s}_i^{-}$ are such that $\sum_{u=1}^{c_i} N_{s_{i,u}|\boldsymbol{s}_{i(m)}^{-}} = 0$), showing that this number is markedly larger for the carbonation nodes. As a consequence, for carbonation, epistemic uncertainty dominates, resulting in wider RIC tolerance intervals and ensuring that the bootstrap-based interval remains a subset of the RIC interval for all $\tau$ (i.e., $\left[\underline{P_C^{boot}}(\tau), \overline{P_C^{boot}}(\tau)\right]_{\gamma}^{\beta} \subseteq \left[\underline{P_C}(\tau), \overline{P_C}(\tau)\right]_{\gamma}^{\beta}$ for each $\tau = 0, \ldots, T_\tau$). Conversely, for chloride ingress, most parent-state combinations are observed (Table 4), leading to comparable widths of the bootstrap and RIC intervals. Finally, for $P_{vio}(\tau)$, the node $V_{DI}(\tau)$ depends on $V_{CD}(\tau)$, which is a logical OR of $P_C(\tau)$ and $P_{Cl}(\tau)$. Since $P_C(\tau)$ is characterized by a wide, prior-driven RIC interval (as explained above), this large epistemic uncertainty propagates to $V_{CD}(\tau)$ and subsequently to $V_{DI}(\tau)$. As a result, $P_{vio}(\tau)$ inherits the behavior of the $P_C(\tau)$, with a wide RIC interval that consistently envelops the narrower bootstrap-based interval.

Table 4. Number of unobserved parent state combinations for $V_C$ and $V_{Cl}$.

| DBN node | Number of unobserved parents state combination (out of $d_i$) | | | DBN node | Number of unobserved parents state combination (out of $d_i$) | | |
|---|---|---|---|---|---|---|---|
| | SSP1 | SSP2 | SSP5 | | SSP1 | SSP2 | SSP5 |
| $V_C(0)$ | *11 (18)* | *11 (18)* | *9 (18)* | $V_{Cl}(0)$ | *2 (9)* | *2 (9)* | *0 (9)* |
| $V_C(1)$ | *28 (36)* | *29 (36)* | *27 (36)* | $V_{Cl}(1)$ | *3 (18)* | *5 (18)* | *0 (18)* |
| $V_C(2)$ | *28 (36)* | *27 (36)* | *27 (36)* | $V_{Cl}(2)$ | *3 (18)* | *2 (18)* | *0 (18)* |
| $V_C(3)$ | *27 (36)* | *20 (36)* | *27 (36)* | $V_{Cl}(3)$ | *1 (18)* | *0 (18)* | *0 (18)* |

| | | | | | | | |
|---|---|---|---|---|---|---|---|
| $V_C(4)$ | *27 (36)* | *18 (36)* | *21 (36)* | $V_{Cl}(4)$ | *0 (18)* | *0 (18)* | *4 (18)* |
| $V_C(5)$ | *27 (36)* | *25 (36)* | *22 (36)* | $V_{Cl}(5)$ | *0 (18)* | *0 (18)* | *3 (18)* |
| $V_C(6)$ | *26 (36)* | *27 (36)* | *23 (36)* | $V_{Cl}(6)$ | *0 (18)* | *0 (18)* | *5 (18)* |
| $V_C(7)$ | *22 (36)* | *20 (36)* | *23 (36)* | $V_{Cl}(7)$ | *0 (18)* | *0 (18)* | *5 (18)* |
| $V_C(8)$ | *18 (36)* | *18 (36)* | *24 (36)* | $V_{Cl}(8)$ | *0 (18)* | *0 (18)* | *6 (18)* |

CC variables enter both carbonation and chloride ingress degradation models (see Appendix A) through the correction factors (for example, $f_T^C(\tau)$ and $f_T^{Cl}(\tau)$ accelerate reaction kinetics and effective diffusivity as temperature increases). As a result, SSP-5 8.5 leads to higher carbonation depths and faster chloride penetration over time compared to SSP-1 2.6 and SSP-2 4.5. In addition, the fact that carbonation depth $x_C(\tau)$ is cumulative with respect to $C_{CO_2}(\tau)$ makes the long-term carbonation process sensitive to the increase of $CO_2$, whose growth is more evident for the SSP-5 8.5. Conversely, in the carbonation physical model, the factor $f_{RH}^C(\tau)$ leads to maximum carbonation rates at intermediate RH values, whereas very low or very high RH reduces effective $CO_2$ transport; in the chloride ingress model, the factor $f_{RH}^{Cl}(\tau)$ increases with RH, so higher RH enhances chloride diffusion. Under the CMIP6 projections for Belgium, the combined evolution of T, RH and $CO_2$ thus produces different sensitivities for the two degradation mechanisms: in periods or scenarios with high RH, chloride penetration is more strongly promoted than carbonation, whereas in drier but warmer conditions carbonation can become more dominant. These interactions, as represented in the DBN through the CC variable nodes, explain the carbonation and chloride exceedance tolerance intervals shown in Fig. 6 and Fig. 7.

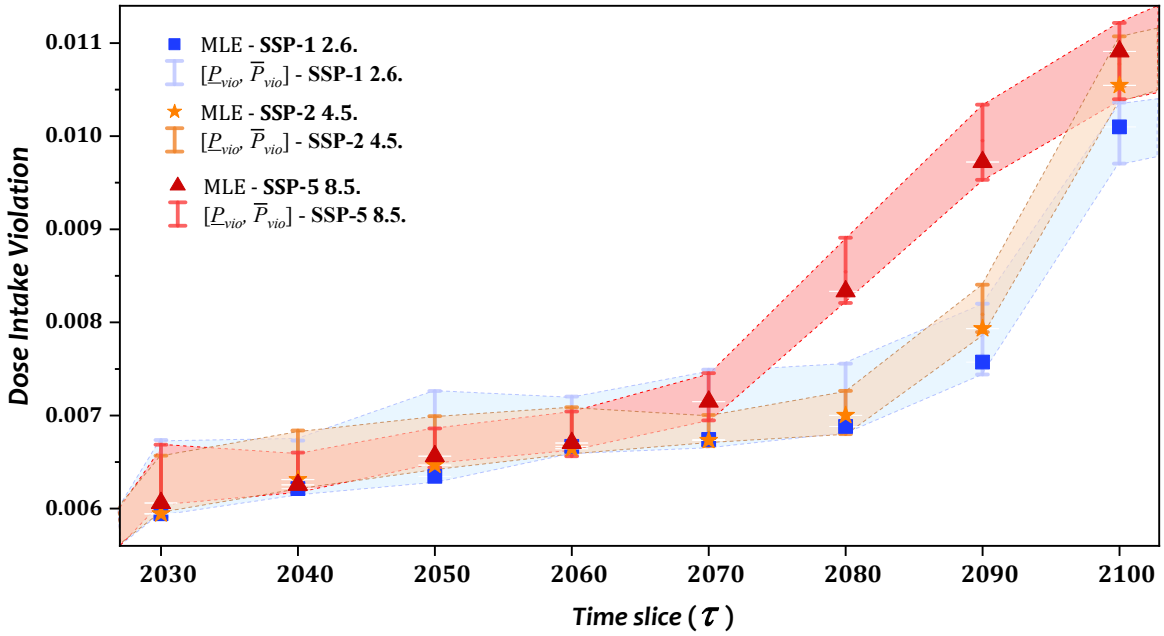


Fig. 9. Dose violation tolerance interval during time slices from 2030-2100 for three climatic projections.

Finally, the residual uncertainty of the *Dose Intake* violation, represented by interval $\left[\underline{P_{vio}}(\tau), \overline{P_{vio}}(\tau)\right]_{\gamma}^{\beta}$, is calculated and plotted in Fig. 9 for each time slice $\tau$ from 2030 to 2100 under scenarios SSP-1 2.6 (blue), SSP-2 4.5 (orange), and SSP-5 8.5 (red). The results indicate that $P_{vio}(\tau)$ increases over time for all SSPs, with SSP-5 8.5 showing the steepest trend. This steeper behavior reflects the compounded effect of the CC drivers: higher temperature and $CO_2$ accelerate the degradation of concrete barriers, whereas RH modulates the relative importance of carbonation versus chloride ingress. These interactions are, then, propagated through the DBN to the dose-intake node. The steeper increase and broader tolerance intervals of $P_{vio}(\tau)$ under SSP-5 8.5 are, therefore, a direct consequence of the more aggressive and more uncertain joint evolution of T, RH, and $CO_2$ in this high-emission scenario.

The upper-bound $\overline{P_{vio}}(\tau)$ consistently exceeds the corresponding point estimate $\hat{P}_{vio}^{MLE}$, which is computed adopting the MLE of parameters $\mathbf{p}^{dat}$ and $\mathbf{p}^{sim}$. The residual uncertainty described by $\left[\underline{P_{vio}}(\tau), \overline{P_{vio}}(\tau)\right]_{\gamma}^{\beta}$ arises from the uncertainty in (C)PT parameters $\mathbf{p}^{dat}$ and $\mathbf{p}^{sim}$. These uncertainties

stem from both the limited number of CC climatic variables model ($N_{dat} = 30$), representing epistemic uncertainty, and the variability associated with the $N_{sim} = 10^4$ simulations of the carbonation and chloride ingress processes. Hence, the width of the tolerance intervals underscores the utility of the proposed methodology in supporting DBN-based PA of NWRs.

From an operational point of view, these results can be directly interpreted in terms of safety design margins and maintenance planning for existing repositories. For each SSP scenario and time slice, the tolerance interval $\left[\underline{P_{vio}}(\tau), \overline{P_{vio}}(\tau)\right]_{\gamma}^{\beta}$ provides a conservative, uncertainty-aware estimate of how close the system may come to exceed the safety target (1 mSv/year). In practice, operators may define risk-informed trigger levels (e.g., a maximum acceptable exceedance probability) and identify the grace time before $\overline{P_{vio}}(\tau)$ approaches or exceeds such levels. This grace time can be used to anticipate the need for mitigation measures (e.g., local strengthening or repair of concrete covers, improvement of drainage to reduce ingress, or implementation of additional engineered barriers), and to prioritise inspection and monitoring campaigns. Because the DBN can theoretically be updated as new monitoring data on climatic variables and FEPs become available, the proposed framework enables an adaptive maintenance strategy in which inspection intervals and mitigation actions are dynamically revised in response to the evolving understanding of both climate change and degradation processes.

## 5. Conclusion

In this work, DBNs have been developed to model concrete degradation within the PA of NWRs. The developed DBN modeling framework allows considering the causal effects of CC climatic variables on the FEPs of the system, accounting and propagating the uncertainty to quantify the residual uncertainty of the safety relevant variables for PA and conducting a dynamic, long-term risk assessment of NWRs. The original methodological contribution consists in the procedure to quantify the impact of the epistemic deep uncertainty in climatic variables arising from CC scenarios and their available models (i.e., CMIP6). By so doing, the framework is suited to:

*i.* account for the time-dependent impact of CC variables relevant to the chemical degradation processes of concrete, i.e., carbonation-induced and chloride ingress corrosion,

*ii.* support CC adaptation decision-making through an uncertainty-aware PA.

In this context, with respect of using traditional PA, DBNs offer the following advantages:

*i.* Considering multi-state variables, which are frequently considered in the PA of NWRs,

*ii.* Capturing the time-evolving nature of PA by explicitly representing the temporal dependencies among FEPs, for instance, the degradation processes in engineered concrete structures under CC scenarios,

*iii.* Updating the results of NWR PA as new evidence becomes available (e.g., from climatic variables or observable FEPs), thus enabling sequential planning strategies in response to CC-induced environmental changes,

*iv.* Overcoming the conservative assumptions inherent in traditional deterministic PA by explicitly accounting for aleatoric and epistemic uncertainties, thereby enabling a realistic probabilistic inference.

A case study has been considered, regarding a near-surface NWR located in Dessel, Belgium, under different CC scenarios (SSP-1 2.6, SSP-2 4.5, SSP-5 8.5). The solely target considered is the probability of dose intake violation, because of the chemical degradation of concrete engineering barriers of NWRs, and specifically because of carbonation-induced corrosion and chloride ingress which are affected by temperature, relative humidity, and $CO_2$ concentration. The results show that when deep uncertainty in CC variables is explicitly modeled, the residual uncertainty in the outcomes increases significantly, e.g., in high-emissions scenarios (SSP-5 8.5). But even in the intermediate SSP-2 4.5 case, the limited CC data leads to wide tolerance intervals and highlights the critical importance of uncertainty quantification for PA.

Although the modeling framework presented can support uncertainty-aware design decisions for a trustworthy PA of NWRs by including the full spectrum of CC-driven uncertainty in long-term risk assessments, some limitations are to be addressed:

- DBN structure is assumed to be fixed and determined through expert elicitation, which neglects structural uncertainty in the causal relationships among variables. This structural uncertainty could significantly contribute to the overall uncertainty associated with dose intake violations. Future work may address this by investigating the use of causal-discovery methods to generate alternative DBN structures and assess their impact on risk outcomes.
- The physics-based degradation models adopted in this work are simplified representations of carbonation and chloride ingress processes. Future work will consider more realistic and comprehensive models that account for additional phenomena, such sulphate attack, or even geochemical weathering of natural barriers, which will require thorough validation against experimental data from laboratory tests and field measurements.
- While computational complexity remains tractable for the current DBN, extending the framework to finer temporal resolutions or additional FEPs could increase the computational burden. Future work will explore approximate inference algorithms [54] to maintain scalability for more complex repository configurations.

## Acknowledgements

The work of Seyed Ali Hosseini, Giovanni Roma and Enrico Zio is supported by PE RETURN SPOKE VS4 (CUPD43C22003030002, codice progetto PE0000005), for the project titled “MULTI RISK SCIENCE FOR RESILIENT COMMUNITIES UNDER A CHANGING CLIMATE”, funded by the NextGenerationEU – Piano Nazionale di Ripresa e Resilienza (PNRR) (Missione 4, componente 2, Investimento 1.3).

# Appendix-A: Concrete degradation models

## A.1. Carbonation-induced corrosion model

Carbon-dioxide ($CO_2$) abundance accelerates the likelihood of carbonation-induced corrosion of concrete structures. The interaction between concrete and atmospheric $CO_2$ results in the formation of calcium carbonate, a phenomenon known as carbonation, which lowers the concrete's alkalinity making the steel of the concrete susceptible to corrosion [10]. Thus, carbonation is quantified by measuring the depth from the concrete surface to the point where alkalinity has reduced to a minimum allowable value. Once carbonation reaches the steel reinforcement, the corrosion propagation phase initiates, leading to expedite the degradation of the concrete structure. In this work, the carbonation depth $x_c(\tau)$ is computed as follows [65, 66, 77]:

$$x_c(\tau) = \sqrt{\frac{2k_{site} f_T^C(\tau) f_{RH}^C(\tau) D_0^C(\tau)^{-n_d}}{a} \int_{\tau_0}^{\tau} C_{CO_2}(\tau)\, dt} \left(\frac{\tau_0}{\tau}\right)^{n_m} \tag{A.1}$$

where $D_0^C$ is the $CO_2$ diffusion coefficient at $\tau_0$, the starting reference year, $n_d$ denotes the aging factor for $D_0^C$, $C_{CO_2}$ is the $CO_2$ mass concentration in the environment $\left(\frac{kg}{m^3}\right)$, $n_m$ is a factor accounting for the exposure to microclimatic wetting and drying cycles (0 for sheltered outdoor, 0.12 for unsheltered outdoor), $a$ is derived from:

$$a = 0.75 C_e C_a O \alpha_H \frac{M_{CO_2}}{M_{C_aO}} \tag{A.2}$$

where $C_e$ is cement content $\left(\frac{kg}{m^3}\right)$, $C_aO$ represents the CaO content in the cement ($\sim$0.65), $M_{CO_2}$ and $M_{C_aO}$ are the molar masses of $CO_2$ $\left(44\frac{kg}{m^3}\right)$ and CaO $\left(56\frac{kg}{m^3}\right)$ respectively, $\alpha_H$ is the degree of hydration, estimated as a function of the water to cement ratio $^W/_C$, as follows:

$$\alpha_H \cong 1 - e^{-3.38^{W}/_{c}} \tag{A.3}$$

to incorporate the effects of climatic variables related to climate change projections, the model is modified considering the factors $f_T^C(\tau)$ and $f_{RH}^C(\tau)$ to account the effects of temperature ($T$), and relative

humidity ($RH$) variations over time, respectively [67]. $k_{site}$ is, also, a related factor for potential $CO_2$ concentrations in industrial sites and urban areas [67]. This analytical model provides a time-dependent corrosion analysis of concrete structures under alternative climate conditions. The dynamic effect of the temperature ($T$) on carbonation depth follows Arrhenius Law [66, 67], where climatic variables impacts the diffusion coefficient, as follow:

$$f_T^C(\tau) = e^{\frac{E}{R}\left[\frac{1}{T_0} - \frac{1}{T(\tau)}\right]} \tag{A.4}$$

where $E$ is the activation energy of the diffusion process $\left(38.3\,\frac{kJ}{mol}\right)$ [68]; $R$ is the gas constant $\left(8.314 \times 10^{-3}\,\frac{kJ}{mol.K}\right)$, and $T_0$, the reference temperature, is usually $293\,K$. The carbonation depth, thus, increases at higher temperatures. For example, the temperature rising during a climate change projection causes an increase in the factor $f_T^C(\tau)$, which then adapts diffusion coefficient over time.

The effect of relative humidity ($RH$), as another climatic variable, has been a subject of consideration for carbonation depth. While some research indicates that $RH$ levels below 30% do not significantly impact carbonation depth [78, 79], it has been found that $RH$ levels above 50% have a notable influence [80]. The factor $f_{RH}^C(\tau)$ considers the influence of $RH$ on diffusion coefficient over time as follows [67]:

$$f_{RH}^C(\tau) = \begin{cases} 0 & if\ RH(\tau) \le 0.25 \\ \left(\dfrac{1 - RH(\tau)^\beta}{1 - RH_0^\beta}\right)^\alpha & otherwise \end{cases} \tag{A.5}$$

Where $RH_0$ is the reference relative humidity, $\alpha$ and $\beta$ are independent parameters of exposure conditions, as reported in [67], i.e., $\alpha = 5$ and $\beta = 2.5$. When $RH$ is larger than $0.65$, the carbonation depth significantly decreases.

## A.2. Chloride-induced corrosion model

The penetration and movement of chloride ions into concrete structures involves the electrochemical dissolution of iron, which can lead to the degradation of concrete barriers. Chloride ingresses into concrete is typically described using a diffusion model, a single mass transport equation for chloride ion

transport. In this work, a time-dependent model is applied, incorporating the chloride diffusion coefficient to estimate the chloride concentration over time [65, 81, 82]. The chloride concentration at a depth $x$ mm and time $\tau$ is:

$$C(x,\tau) = C_0^{Cl}\left[1 - erf\left(\frac{x}{2\sqrt{k_e k_t k_c f_T^{Cl}(\tau) f_{RH}^{Cl}(\tau) D_0^{Cl}\left(\frac{\tau_0}{\tau}\right)^n \tau}}\right)\right] \quad \text{(A.6)}$$

Where $C_0^{Cl}$ denotes the Chloride ion concentration on the surface; $D_0^{Cl}$ is the reference diffusion coefficient; $n$ is aging factor for $D_0^{Cl}$. $k_e$ is the environmental coefficient, $k_t$ is the test method factor, and $k_c$ is curing factor. Like carbonation depth process, $f_T^{Cl}(\tau)$ and $f_{RH}^{Cl}(\tau)$ are both factors related to environmental exposure variables, temperature ($T$) and relative humidity ($RH$), respectively. $f_T^{Cl}(\tau)$ has the same formula as well as $f_T^{C}(\tau)$ in Eq. A.4, while $f_{RH}^{Cl}(\tau)$ is defined as follows [83]:

$$f_{RH}^{Cl}(\tau) = \left(1 + \frac{(1 - RH(\tau))^4}{(1 - RH_0)^4}\right)^{-1} \quad \text{(A.7)}$$

The surface chloride boundaries, $C_0^{Cl}$, can be categorized into specific exposure zones such as submerged, splash, tidal, and atmospheric zones. For instance, $C_0^{Cl} = 1.15\frac{kg}{m^3}$ is typical for atmospheric zone, which is far from the coast, whereas the chloride concentrations are more severe in coastal and tidal environments [84]. CC, thus, has the potential to impact chloride penetration into the concrete through related changes in $T$and $RH$, which are incorporated in $f_T^{Cl}(\tau)$ and $f_{RH}^{Cl}(\tau)$. The following section aims to provide results in different climatic projections.

## References


1. Chapman, N.A. and I.G. Mc Kinley, *The geological disposal of nuclear waste.* 1987.
2. Cadini, F., et al., *Monte Carlo-based assessment of the safety performance of a radioactive waste repository.* Reliability Engineering & System Safety, 2010. **95**(8): p. 859-865.
3. Brown, J., et al., *Overview of the MODARIA programme (and comments on implications for future programmes of work).* Journal of Radiological Protection, 2022. **42**(2): p. 020505.
4. Lee, H., et al., *IPCC, 2023: Climate Change 2023: Synthesis Report, Summary for Policymakers. Contribution of Working Groups I, II and III to the Sixth Assessment Report of the*

*Intergovernmental Panel on Climate Change [Core Writing Team, H. Lee and J. Romero (eds.)]. IPCC, Geneva, Switzerland.* 2023.
5. Chang, I., *A Comparison Study of the Performance Assessment Probabilistic Risk Assessment and Vulnerability Assessment Methodologies*. 2006, Sandia National Lab.(SNL-NM), Albuquerque, NM (United States).
6. Yim, M.-S. and S.A. Simonson, *Performance assessment models for low level radioactive waste disposal facilities: a review.* Progress in Nuclear Energy, 2000. **36**(1): p. 1-38.
7. Zio, E. and G. Apostolakis, *Two methods for the structured assessment of model uncertainty by experts in performance assessments of radioactive waste repositories.* Reliability Engineering & System Safety, 1996. **54**(2-3): p. 225-241.
8. Tosoni, E., A. Salo, and E. Zio, *Scenario analysis for the safety assessment of nuclear waste repositories: A critical review.* Risk Analysis, 2018. **38**(4): p. 755-776.
9. Cadini, F., A. Gioletta, and E. Zio, *Improved metamodel-based importance sampling for the performance assessment of radioactive waste repositories.* Reliability Engineering & System Safety, 2015. **134**: p. 188-197.
10. Glasser, F.P., J. Marchand, and E. Samson, *Durability of concrete—Degradation phenomena involving detrimental chemical reactions.* Cement and concrete research, 2008. **38**(2): p. 226-246.
11. Li, K., F. Zhao, and Y. Zhang, *Influence of carbonation on the chloride ingress into concrete: Theoretical analysis and application to durability design.* Cement and Concrete Research, 2019. **123**: p. 105788.
12. Helton, J.C., *Uncertainty and sensitivity analysis techniques for use in performance assessment for radioactive waste disposal.* Reliability Engineering & System Safety, 1993. **42**(2-3): p. 327-367.
13. Helton, J.C. and A. Shiver, *A Monte Carlo procedure for the construction of complementary cumulative distribution functions for comparison with the EPA release limits for radioactive waste disposal.* Risk Analysis, 1996. **16**(1): p. 43-55.
14. Vesely, W.E., et al., *Fault tree handbook*. 1981.
15. PORTtONS, O., *PRA PROCEDURES GUIDE.* 1983.
16. Tosoni, E., et al., *Comprehensiveness of scenarios in the safety assessment of nuclear waste repositories.* Reliability Engineering & System Safety, 2019. **188**: p. 561-573.
17. Hosseini, S.A., F. Di Maio, and E. Zio. *A Dynamic Bayesian Network for the Performance Assessment of Nuclear Waste Repositories Undergoing Chemical Degradation due to Climate Change*. in *2024 8th International Conference on System Reliability and Safety (ICSRS)*. 2024. IEEE.
18. Yodo, N., P. Wang, and Z. Zhou, *Predictive resilience analysis of complex systems using dynamic Bayesian networks.* IEEE Transactions on Reliability, 2017. **66**(3): p. 761-770.
19. An, X., et al., *An integrated resilience assessment methodology for emergency response systems based on multi-stage STAMP and dynamic Bayesian networks.* Reliability Engineering & System Safety, 2023. **238**: p. 109445.
20. Kammouh, O., P. Gardoni, and G.P. Cimellaro, *Probabilistic framework to evaluate the resilience of engineering systems using Bayesian and dynamic Bayesian networks.* Reliability Engineering & System Safety, 2020. **198**: p. 106813.
21. Junyung, K., et al., *System risk quantification and decision making support using functional modeling and dynamic Bayesian network.* Reliability Engineering & System Safety, 2021. **215**: p. 107880.
22. Delikhoon, M., et al., *Towards decision-making support for complex socio-technical system safety assessment: a hybrid model combining FRAM and dynamic Bayesian networks.* Process Safety and Environmental Protection, 2024. **187**: p. 776-791.
23. Zinetullina, A., et al., *Quantitative resilience assessment of chemical process systems using functional resonance analysis method and Dynamic Bayesian network.* Reliability Engineering & System Safety, 2021. **205**: p. 107232.

24. Di Maio, F., S. Marchetti, and E. Zio, *A framework of sensitivity analysis for the performance assessment of safety barriers impacted by NaTech accidents.* Process Safety and Environmental Protection, 2023. **171**: p. 1022-1030.
25. Di Maio, F., S. Marchetti, and E. Zio, *Robust multi-objective optimization of safety barriers performance parameters for NaTech scenarios risk assessment and management.* Reliability Engineering & System Safety, 2023. **235**: p. 109245.
26. Morato, P.G., et al., *Optimal inspection and maintenance planning for deteriorating structural components through dynamic Bayesian networks and Markov decision processes.* Structural Safety, 2022. **94**: p. 102140.
27. Mancuso, A., et al., *Portfolio optimization of safety measures for the prevention of time-dependent accident scenarios.* Reliability Engineering & System Safety, 2019. **190**: p. 106500.
28. Pinciroli, L., et al., *Risk Assessment for Modern Industry.* Reliability Engineering & System Safety, 2025: p. 112126.
29. Zhao, X., X. Wang, and M.W. Golay, *Bayesian network–based fault diagnostic system for nuclear power plant assets.* Nuclear Technology, 2023. **209**(3): p. 401-418.
30. Podofillini, L., B. Reer, and V.N. Dang, *A traceable process to develop Bayesian networks from scarce data and expert judgment: A human reliability analysis application.* Reliability Engineering & System Safety, 2023. **230**: p. 108903.
31. Liu, J., et al., *A Bayesian belief network framework for nuclear power plant human reliability analysis accounting for dependencies among performance shaping factors.* Reliability Engineering & System Safety, 2022. **228**: p. 108766.
32. Segarra, J.D., M. Bensi, and M. Modarres, *A Bayesian network approach for modeling dependent seismic failures in a nuclear power plant probabilistic risk assessment.* Reliability Engineering & System Safety, 2021. **213**: p. 107678.
33. Segarra, J.D., M. Bensi, and M. Modarres, *Multi-unit seismic probabilistic risk assessment: A Bayesian network perspective.* Reliability Engineering & System Safety, 2023. **234**: p. 109169.
34. Roma, G., F. Di Maio, and E. Zio, *A condition-informed dynamic Bayesian network framework to support severe accident management in nuclear power plants.* Reliability Engineering & System Safety, 2024. **252**: p. 110437.
35. Roma, G., F. Di Maio, and E. Zio, *Decision Making Under Uncertainty by Trustworthy Dynamic Bayesian Networks for Severe Accident Management in Nuclear Power Plants.* Reliability Engineering & System Safety, 2025: p. 111793.
36. Guo, H. and Y. Dong, *Dynamic Bayesian network for durability of reinforced concrete structures in long-term environmental exposures.* Engineering Failure Analysis, 2022. **142**: p. 106821.
37. Cai, B., et al., *Resilience evaluation methodology of engineering systems with dynamic-Bayesian-network-based degradation and maintenance.* Reliability Engineering & System Safety, 2021. **209**: p. 107464.
38. Molaioni, F., C.P. Andriotis, and Z. Rinaldi, *Life-cycle fragility analysis of aging reinforced concrete bridges: A dynamic Bayesian network approach.* Structural Safety, 2025: p. 102654.
39. Poropudas, J. and K. Virtanen, *Simulation metamodeling with dynamic Bayesian networks.* European Journal of Operational Research, 2011. **214**(3): p. 644-655.
40. Mkrtchyan, L., L. Podofillini, and V.N. Dang, *Methods for building Conditional Probability Tables of Bayesian Belief Networks from limited judgment: An evaluation for Human Reliability Application.* Reliability Engineering & System Safety, 2016. **151**: p. 93-112.
41. Murphy, K., *Dynamic Bayesian Networks: Representation, Inference and Learning*. 2002.
42. Jacob, D., et al., *Regional climate downscaling over Europe: perspectives from the EURO-CORDEX community.* Regional environmental change, 2020. **20**: p. 1-20.
43. Jacobeit, J., et al., *Statistical downscaling for climate change projections in the Mediterranean region: methods and results.* Regional environmental change, 2014. **14**: p. 1891-1906.
44. O'Neill, B.C., et al., *The scenario model intercomparison project (ScenarioMIP) for CMIP6.* Geoscientific Model Development, 2016. **9**(9): p. 3461-3482.

45. Tang, S.W., et al., *Recent durability studies on concrete structure.* Cement and Concrete Research, 2015. **78**: p. 143-154.
46. Hawkins, E. and R. Sutton, *The potential to narrow uncertainty in regional climate predictions.* Bulletin of the American Meteorological Society, 2009. **90**(8): p. 1095-1108.
47. O'Neill, B.C., et al., *A new scenario framework for climate change research: the concept of shared socioeconomic pathways.* Climatic Change, 2014. **122**(3): p. 387-400.
48. Rohmer, J., *Uncertainties in conditional probability tables of discrete Bayesian Belief Networks: A comprehensive review.* Engineering Applications of Artificial Intelligence, 2020. **88**: p. 103384.
49. Campos, C.P.D. and F.G. Cozman, *The inferential complexity of Bayesian and credal networks*, in *Proceedings of the 19th international joint conference on Artificial intelligence*. 2005, Morgan Kaufmann Publishers Inc.: Edinburgh, Scotland. p. 1313–1318.
50. Mauá, D.D. and F.G. Cozman, *Thirty years of credal networks: Specification, algorithms and complexity.* International Journal of Approximate Reasoning, 2020. **126**: p. 133-157.
51. Tosoni, E., F. Di Maio, and E. Zio. *Identification of FEP critical paths from a Bayesian network model for the risk assessment of nuclear waste repositories*. in *Proceedings of the 30th European Safety and Reliability Conference and the 15th Probabilistic Safety Assessment and Management Conference*. 2020. Research Publishing, Singapore.
52. Tosoni, E., *Novel methods of scenario analysis for the probabilistic risk assessment of nuclear waste storage and disposal facilities.* 2021.
53. *Climate Data Store (CDS)*. Available from: **https://cds.climate.copernicus.eu/datasets/projections-cmip6?tab=overview**.
54. Koller, D. and N. Friedman, *Probabilistic Graphical Models - Principles and Techniques*. 2009: MIT Press. I-XXXV.
55. Hamza, Z. and T. Abdallah. *Mapping Fault Tree into Bayesian Network in safety analysis of process system*. in *2015 4th International Conference on Electrical Engineering (ICEE)*. 2015.
56. Khakzad, N., F. Khan, and P. Amyotte, *Dynamic safety analysis of process systems by mapping bow-tie into Bayesian network.* Process Safety and Environmental Protection, 2013. **91**(1): p. 46-53.
57. Kim, J., et al., *System risk quantification and decision making support using functional modeling and dynamic Bayesian network.* Reliability Engineering & System Safety, 2021. **215**: p. 107880.
58. Heckerman, D., D. Geiger, and D.M. Chickering, *Learning Bayesian networks: The combination of knowledge and statistical data.* Machine learning, 1995. **20**: p. 197-243.
59. Guba, A., M. Makai, and L. Pál, *Statistical aspects of best estimate method—I.* Reliability engineering & system safety, 2003. **80**(3): p. 217-232.
60. Tosoni, E., et al., *Definition of the data for comprehensiveness in scenario analysis of near-surface nuclear waste repositories.* Data in Brief, 2020. **31**: p. 105780.
61. Phung, Q.T., N. Maes, and D. Jacques, *Current concerns on durability of concrete used in nuclear power plants and radioactive waste repositories*, in *Congrès International de Géotechnique–Ouvrages–Structures*. 2017, Springer. p. 1107-1121.
62. Seetharam, S., et al., *Model assumptions for the cementitious near field of the Dessel near surface repository.* ONDRAF/NIRAS, Brussels, Belgium, 2012.
63. Brodén, K., et al., *Experiences of storage of radioactive waste packages in the Nordic countries*. 2001, Nordisk Kernesikkerhedsforskning, Roskilde (Denmark).
64. BayesFusion, L., *Genie modeler.* User Manual. Available online: **https://support**. bayesfusion. com/docs/(accessed on 21 October 2019), 2017. **16**: p. 30-32.
65. Stewart, M.G., X. Wang, and M.N. Nguyen, *Climate change impact and risks of concrete infrastructure deterioration.* Engineering Structures, 2011. **33**(4): p. 1326-1337.
66. Yoon, I.-S., O. Çopuroğlu, and K.-B. Park, *Effect of global climatic change on carbonation progress of concrete.* Atmospheric environment, 2007. **41**(34): p. 7274-7285.
67. Bastidas-Arteaga, E., et al. *Multi-region lifetime assessment of reinforced concrete structures subjected to carbonation and climate change*. in *Structures*. 2022. Elsevier.

68. Ramani, V. and L. Zhang, *Impacts of climate change on long-term reliability of reinforced concrete structures due to chloride ingress.* Construction and Building Materials, 2022. **354**: p. 129091.
69. Nasr, A., D. Honfi, and O. Larsson Ivanov, *Probabilistic analysis of climate change impact on chloride-induced deterioration of reinforced concrete considering Nordic climate.* Journal of Infrastructure Preservation and Resilience, 2022. **3**(1): p. 8.
70. Choe, D.-E., et al., *Seismic fragility estimates for reinforced concrete bridges subject to corrosion.* Structural Safety, 2009. **31**(4): p. 275-283.
71. Chateauneuf, A., A. Messabhia, and A. Ababneh, *Reliability analysis of corrosion initiation in reinforced concrete structures subjected to chlorides in presence of epistemic uncertainties.* Structural Safety, 2020. **86**: p. 101976.
72. Matteo, F., et al., *Time-dependent reliability analysis of the reactor building of a nuclear power plant for accounting of its aging and degradation.* Reliability Engineering & System Safety, 2021. **205**: p. 107173.
73. Hosseini, S.A., et al., *A parametric statistical inference measure for input-based uncertainty quantification in BEPU analysis.* Annals of Nuclear Energy, 2025. **214**: p. 111214.
74. De Campos, C.P. and F.G. Cozman. *The inferential complexity of Bayesian and credal networks*. in *IJCAI*. 2005. Citeseer.
75. Gujar, R. and V. Vakharia, *Prediction and validation of alternative fillers used in micro surfacing mix-design using machine learning techniques.* Construction and Building Materials, 2019. **207**: p. 519-527.
76. Vakharia, V. and R. Gujar, *Prediction of compressive strength and portland cement composition using cross-validation and feature ranking techniques.* Construction and Building Materials, 2019. **225**: p. 292-301.
77. Bastidas-Arteaga, E., et al., *Influence of global warming on durability of corroding RC structures: A probabilistic approach.* Engineering Structures, 2013. **51**: p. 259-266.
78. Russell, D., et al., *Effect of relative humidity and air permeability on prediction of the rate of carbonation of concrete.* Proceedings of the Institution of Civil Engineers-Structures and Buildings, 2001. **146**(3): p. 319-326.
79. Al-Khaiat, H. and N. Fattuhi, *Carbonation of concrete exposed to hot and arid climate.* Journal of materials in civil engineering, 2002. **14**(2): p. 97-107.
80. Bary, B. and A. Sellier, *Coupled moisture—carbon dioxide–calcium transfer model for carbonation of concrete.* Cement and concrete research, 2004. **34**(10): p. 1859-1872.
81. Kwon, S.J., et al., *Service life prediction of concrete wharves with early-aged crack: Probabilistic approach for chloride diffusion.* Structural Safety, 2009. **31**(1): p. 75-83.
82. Luping, T. and J. Gulikers, *On the mathematics of time-dependent apparent chloride diffusion coefficient in concrete.* Cement and concrete research, 2007. **37**(4): p. 589-595.
83. El Hassan, J., et al., *Reliability-based assessment of the effect of climatic conditions on the corrosion of RC structures subject to chloride ingress.* Engineering Structures, 2010. **32**(10): p. 3279-3287.
84. Val, D.V. and M.G. Stewart, *Life-cycle cost analysis of reinforced concrete structures in marine environments.* Structural safety, 2003. **25**(4): p. 343-362.